NAVAL POSTGRADUATE SCHOOL

MONTEREY, CALIFORNIA

THESIS

MULTISCALE MODELING OF BONE

by

Brandon R. Clumpner

December 2014

Thesis Advisor: Young W. Kwon
Second Reader: Jarema M. Didoszak

Approved for public release; distribution is unlimited

THIS PAGE INTENTIONALLY LEFT BLANK

REPORT DOCUMENTATION PAGE

Form Approved OMB No. 0704–0188

1. AGENCY USE ONLY *(Leave blank)*	2. REPORT DATE	3. REPORT TYPE AND DATES COVERED
	December 2014	Master's Thesis

4. TITLE AND SUBTITLE
MULTISCALE MODELING OF BONE

5. FUNDING NUMBERS

6. AUTHOR Brandon R. Clumpner

7. PERFORMING ORGANIZATION NAME(S) AND ADDRESS(ES)
Naval Postgraduate School
Monterey, CA 93943–5000

8. PERFORMING ORGANIZATION REPORT NUMBER

9. SPONSORING /MONITORING AGENCY NAME(S) AND ADDRESS(ES)
N/A

10. SPONSORING/MONITORING AGENCY REPORT NUMBER

11. SUPPLEMENTARY NOTES The views expressed in this thesis are those of the author and do not reflect the official policy or position of the Department of Defense or the U.S. Government. IRB Protocol number ____N/A____.

12a. DISTRIBUTION / AVAILABILITY STATEMENT
Approved for public release; distribution is unlimited

12b. DISTRIBUTION CODE

13. ABSTRACT (maximum 200 words)

A multiscale model was developed to link the hierarchies of human bone in different length scales. Bone has a unique structure displaying large stiffness with minimal weight. This is achieved through a hierarchy of complex geometries composed of only three materials: hydroxyapatite, collagen and water.

The identifiable structures of bone are hydroxyapatite, tropocollagen, fibrils, fibers, lamellar layers, trabecular bone, cancellous bone and cortical bone. A spring model was used to evaluate the stiffness of collagen. A unit-cell based micromechanics model analyzed both the normal and shear properties of fibrils, fibers, and lamellar layers. A layered composite model assessed cortical and trabecular bone while a simple finite element model was used to evaluate cancellous bone.

Modeling bone from nanoscale components to macroscale structures allows the influence of each structure to be assessed. It was found that the distribution of hydroxyapatite within the tropocollagen matrix at the fibril level influences the macroscale properties the most. Additionally, the model allows perturbations to the geometry of any hierarchy to be analyzed. With so little known about the detailed structure of nanoscale and microscale bone, a model comprising the complete hierarchy of bone can be used to help validate assumptions or hypotheses about structure.

14. SUBJECT TERMS	15. NUMBER OF PAGES
multiscale modeling, biocomposite, biomaterials, tropocollagen, collagen, bone, hydroxyapatite, FEM, tetrakaidecahedron, fibril, trabecular, cancellous, cortical	123
	16. PRICE CODE

17. SECURITY CLASSIFICATION OF REPORT	18. SECURITY CLASSIFICATION OF THIS PAGE	19. SECURITY CLASSIFICATION OF ABSTRACT	20. LIMITATION OF ABSTRACT
Unclassified	Unclassified	Unclassified	UU

NSN 7540–01–280–5500

Standard Form 298 (Rev. 2–89)
Prescribed by ANSI Std. 239–18

THIS PAGE INTENTIONALLY LEFT BLANK

Approved for public release; distribution is unlimited

MULTISCALE MODELING OF BONE

Brandon R. Clumpner
First Lieutenant, United States Army
B.S.M.E., United States Military Academy, 2013

Submitted in partial fulfillment of the
requirements for the degrees of

MASTER OF SCIENCE IN MECHANICAL ENGINEERING

and

MECHANICAL ENGINEER

from the

NAVAL POSTGRADUATE SCHOOL
December 2014

Author: Brandon R. Clumpner

Approved by: Young W. Kwon
Thesis Advisor

Jarema M. Didoszak
Second Reader

Garth V. Hobson
Chair, Department of Mechanical and Aerospace Engineering

THIS PAGE INTENTIONALLY LEFT BLANK

ABSTRACT

A multiscale model was developed to link the hierarchies of human bone in different length scales. Bone has a unique structure displaying large stiffness with minimal weight. This is achieved through a hierarchy of complex geometries composed of only three materials: hydroxyapatite, collagen and water.

The identifiable structures of bone are hydroxyapatite, tropocollagen, fibrils, fibers, lamellar layers, trabecular bone, cancellous bone and cortical bone. A spring model was used to evaluate the stiffness of collagen. A unit-cell based micromechanics model analyzed both the normal and shear properties of fibrils, fibers, and lamellar layers. A layered composite model assessed cortical and trabecular bone while a simple finite element model was used to evaluate cancellous bone.

Modeling bone from nanoscale components to macroscale structures allows the influence of each structure to be assessed. It was found that the distribution of hydroxyapatite within the tropocollagen matrix at the fibril level influences the macroscale properties the most. Additionally, the model allows perturbations to the geometry of any hierarchy to be analyzed. With so little known about the detailed structure of nanoscale and microscale bone, a model comprising the complete hierarchy of bone can be used to help validate assumptions or hypotheses about structure.

THIS PAGE INTENTIONALLY LEFT BLANK

TABLE OF CONTENTS

THIS PAGE INTENTIONALLY LEFT BLANK

LIST OF FIGURES

THIS PAGE INTENTIONALLY LEFT BLANK

LIST OF TABLES

THIS PAGE INTENTIONALLY LEFT BLANK

LIST OF ACRONYMS AND ABBREVIATIONS

4KDH	tetrakaidecahedron
BSP	bone sialoprotein
BV/TV	bone volume / tissue volume
EFM	extrafibrillar mineralization
FEM	finite element method
Gly	glycine
HA	hydroxyapatite
HCP	hexagonal close-packed
Hyp	hydroxyproline
NCP	non-collagenous proteins
PPII	polyproline-II
Pro	proline
SR-PNT	synchrotron X-ray phase nano-tomography
SSV	serial surface view
Tb.Th	trabecular thickness
TC	tropocollagen

THIS PAGE INTENTIONALLY LEFT BLANK

ACKNOWLEDGMENTS

I would like to thank my advisor, Prof. Kwon, for his guidance and motivation. Also, I would like to thank my friends and family for their support throughout the writing process.

THIS PAGE INTENTIONALLY LEFT BLANK

I. INTRODUCTION

Biomaterials are complex living tissues that have developed through evolutionary processes. They are distinct for their complex hierarchies built by simple materials [1]. There are a limited number of structural materials in the human body, but living organisms rely on composite hierarchical structures to achieve macroscale form and function [2]. Biomaterials such as skin, ligaments, tendons, muscles and bones exhibit this hierarchical organization. This study will focus on the structure of bone.

Bone is the main structural component of the body. It supports the compressive loads of our body weight, serves as lever arms to transmit muscle contractions to movement and provides rigidity for each limb [3]–[6]. Unlike tendons and ligaments, bone structures support compressive loads, as well as bending, torsional and shearing loads [5]. Bone structure has evolved, adhering to the biological adage that form follows function. Bone's complex hierarchies create a load bearing structure of minimal weight, capable of supporting enormous loads [4]. Additionally, bone serves as the storage site for bone marrow, calcium and phosphate [3], [5]. In order to understand the structural properties of bone, a multi-scale model will be presented. This model will begin at the nano level and continue up the hierarchies to the macroscale level; however, for descriptive purposes, bone will be introduced from the macroscale down.

A. MACROSCALE BONE

There are five types of bones in the human body: long, short, flat, sesamoid and irregular [6]. Long, short, and flat bones are described by their names. Sesamoid bones exist within a tendon, such as the patella. Irregular bones, examples being vertebrae, fit into none of the other categories [6]. Bones are composed of two distinct types of bone: woven bone and lamellar bone [3], [7]. Woven bone is a disordered array of collagen fibrils [8]. Lamellar bone, which is organized into distinct sheets, is an ordered array of bone fibers in a matrix material [1]. It is the dominant form of bone and closely resembles a layered fiber-reinforced composite [9].

Lamellar bone can be further divided into two bone structures: cortical bone and cancellous bone [7], [10]. Cortical bone, also known as compact bone, is a dense form of bone. It is composed of concentric layers of lamellar bone with varying fiber directions [3]. The stacking of concentric layers forms an osteon, or Haversian system, and is the representative subunit of cortical bone [5]. They contain a Haversian canal, which supplies the blood and nerve endings to bone, at their center. Additionally, there are bone cells named osteoblasts that form new bone and matrix material [11]. These are interconnected by a network of canaliculi that help transport necessary nutrients and waste materials in the compact bone structures [9]. These osteons are densely packed in cortical bone.

Cancellous bone, otherwise known as spongy or trabecular bone, is a very porous material [3], [10]. Cancellous bone is very similar in form to metal foam; it is a complex array of rods and thin plates. These rods are known as trabeculae and are composed of lamellar bone. The material of trabeculae will be referred to as trabecular bone while the material of cancellous bone as a macroscale material will be referred to as cancellous bone. The lamellar bone of a trabecula has a uniform fiber direction along the axis of the structure [9]. This is caused by the constant absorption and re-growth of lamellar material as a direct result of the stresses applied to the bone [4], [9].

Cortical bone is predominantly found at the cortex of bones and along the long axis of long bones. It accounts for almost 80% of the skeletal system's weight. Cancellous bone is present along the inner radius of long bones, within the heads of long bones, and acts as filler under the cortex of cortical bone. Cancellous bone also regulates the metabolic functions executed by bone.

B. MICROSCALE BONE

The lamellae of both cortical bone and trabecular bone are composed of two microstructures: fibrils and fibers [3]. Bone fibrils are an extremely ordered array of bone mineral and tropocollagen (TC) molecules [2], [12]–[13]. The bone mineral present within fibrils is classified as intrafibrillar mineral. TC molecules form a lattice structure

that is reinforced by the bone minerals [13]. The fibril material is representative of a particle reinforced composite [1].

Bone fibers are an ordered array of mineralized fibrils [12]. The individual fibrils are surrounded by a coating of bone mineral known as extrafibrillar mineral [3], [14]. These fibers are not independent structures, but exist only within the complex lamellar bone [13], similar to a fiber reinforced composite [12]. Additionally, the fibers are surrounded by an extrafibrillar matrix that contains the cells and non-structural proteins necessary for metabolic functions [4].

C. NANOSCALE BONE

Bone is almost entirely composed of two materials: hydroxyapatite (HA) and collagen [3]. HA, also known as bone mineral, is a small, thin, plate structure with a large elastic modulus [4], [9]. The collagen species of bone is 95% collagen I and a 5% assortment of other collagen species. The main constituent of collagen I are TC molecules. TC molecules are a triple helix molecule [8] composed of three polyproline II helices [11].

D. HIERARCHICAL OVERVIEW

From just three basic materials, HA, TC, and water, a complex hierarchy of bone is built. This structure has evolved, and continues to evolve, to support the stresses it encounters [4]. The astounding aspect of bone is that its material properties have been produced through the complex geometry of simple materials [9]. This hierarchy is broken down and visualized in Figure 1.

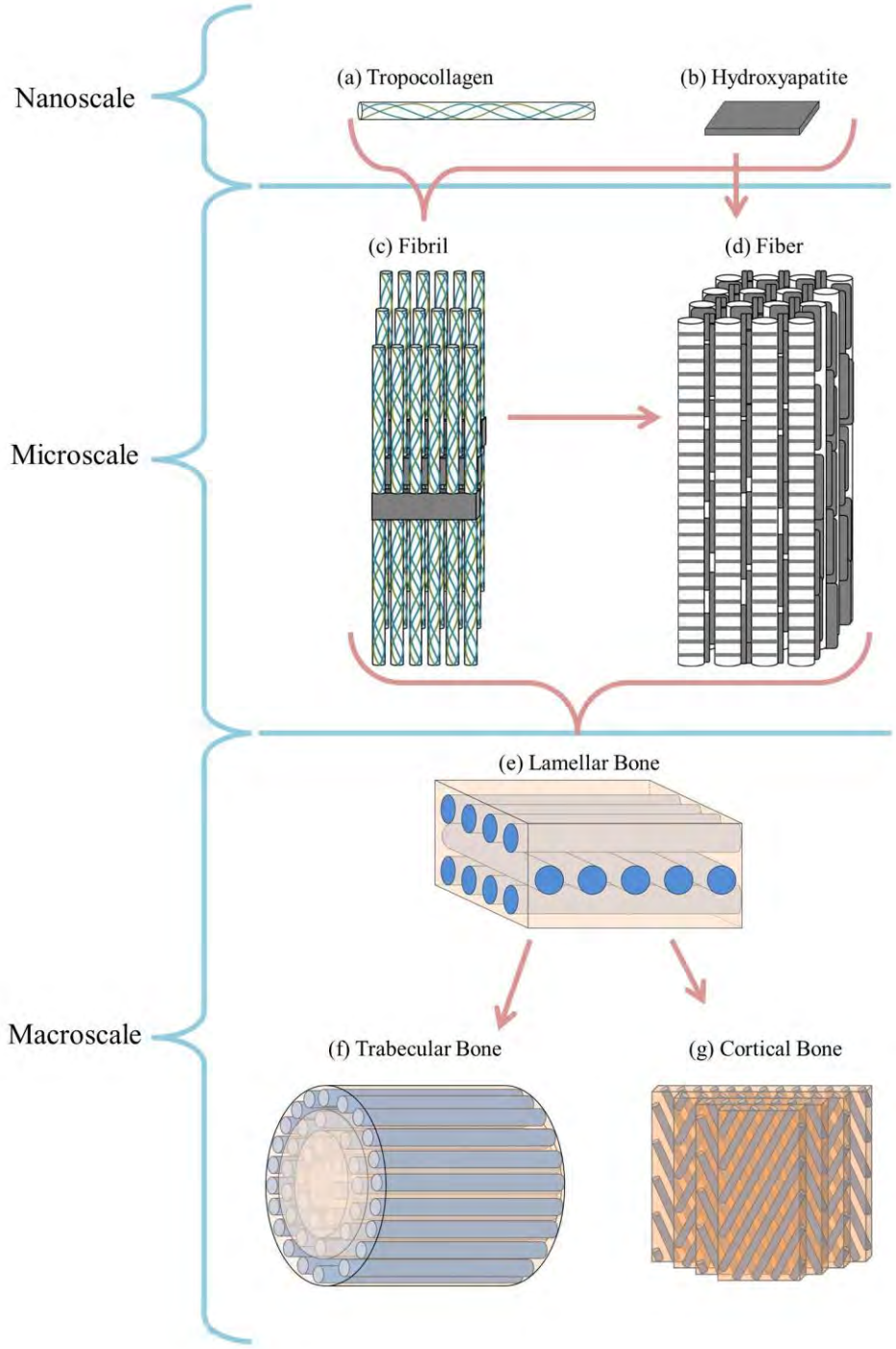

Figure 1. Bone hierarchies as classified into nanoscale (a–b), microscale (c–d), and macroscale (e–g) structures. (a) Tropocollagen molecules comprised of three polyproline II helices. (b) Hydroxyapatite crystals. (c) Organized fibril lattice structures. (d) Mineralized fibers. (e) Lamellar bone constructed of layered fibrils in a matrix. (f) Trabecular bone with parallel fiber layers. (g) Cortical bone with alternating fiber orientations

II. NANOSCALE

The main structural nano components of bone are hydroxyapatite and tropocollagen. These two materials serve as the building blocks for the subsequent layers. In addition to hydroxyapatite (HA) and tropocollagen (TC) there are microscopic inclusions of non-collagenous proteins (NCPs) and proteoglycans. The NCPs serve metabolic functions and, along with the proteoglycans, act as a matrix filler [9]. Since the NCPs and proteoglycans serve no mechanical functions and comprise a small volume percentage, they are ignored in this study. The following chapter will describe in detail HA and TC, and will propose a mechanical model for the TC structure.

A. HYDROXYAPATITE

HA is a crystalline solid composed of calcium phosphate. It is the only ceramic material created naturally within the body [8], [15]. HA is sometimes referred to as the mineral phase, or bone mineral, and takes a polycrystalline form as small thin plates within the body [4], [16]. HA is the direct cause of the stiffness associated with bone.

1. Chemistry

The chemical formula of HA is $Ca_{10}(PO_4)_6(OH)_2$ [8]. The growth of HA is regulated by heterogeneous nucleation factors, which are thought to be concentrated within the gap zones [4]. These nucleation factors promote the growth of the mineral phase and contribute to the highly ordered structure of the micro-level hierarchy of bone. Additionally, HA exhibits a hexagonal close-packed (HCP) crystal lattice. A single crystal can be grown in a lab and tested to determine material properties [16]. The HCP crystal lattice of HA is shown in Figure 2.

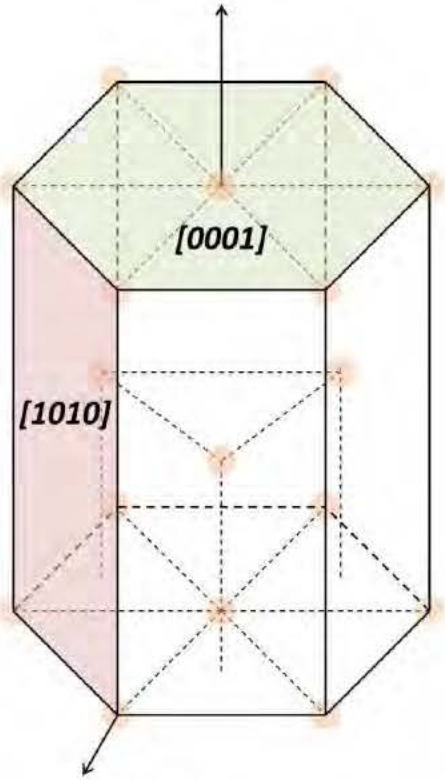

Figure 2. Hydroxyapatite crystal lattice structure: hexagonal close-packed.

2. Material Properties

From nanoindentation testing completed on single HA crystals, the stiffness in the [0001] direction was found to be greater than in the [1010] direction [16]. The results of these tests are shown in Table 1, along with several other experimental results.

Table 1. Hydroxyapatite material values.

Direction	E [GPa]	ν	Source
[0001]	150.38		Nanoindentation [16]
[1010]	143.56		Nanoindentation [16]
	114	0.27	Ultrasonic [17]
	165		[8]

The results from [17] are representative of ultrasonic moduli testing completed on pure powdered materials. These results assumed an isotropic material in pure

polycrystalline form. The estimates from [8] cite no methods or sources. The values from the nanoindentation experiments will be used in this study.

Furthermore, the HCP structures are organized into small plates ranging from 1.5–5 nm thick [9]. Although the size of HA crystals vary based on location, mineral density and time allowed for growth, the average crystal size is widely agreed upon at 50 nm $\times$ 25 nm $\times$ 3 nm [1], [3], [4], [8], [16], [18], [19].

3. Non-structural Function

In addition to providing structural support to the skeletal system, HA serves as the storage site for ions [16]. HA is responsible for 99%, 90%, 90% and 50% of the body's store of calcium, phosphorus, sodium and magnesium, respectively [4]. HA has a large surface area to volume ratio, allowing for rapid absorption and dissolution when ions are needed [4], [16]. This relationship is important in determining effects of bone diseases and disorders that affect bone density and calcium absorption.

B. TROPOCOLLAGEN

The tropocollagen molecule is the basic molecular unit of collagen. There are 28 different variations of collagen; each is used for a different physiological purpose within the body [20]. Collagen I is the main collagen species found in bone, comprising 95% of the total collagen [21].

1. Tropocollagen Structure

Collagen I is composed of three helical protein strands: two alpha-1 type-1 strands and one alpha-1 type-2 strand [20], [22]–[26]. Each strand differs in its amino acid sequence, but each maintains a similar helical structure. Both alpha-1 type-1 and alpha-1 type-2 are left handed polyproline II helices, are 300 nm long, and contain approximately 1000 amino acids [11], [22], [26]–[32]. Additionally, the polyproline-II (PPII) helices of the alpha-1 type-1 and alpha-1 type-2 collagen contain a common repeating subunit: Gly-X-Y [20], [23]–[25], [27], [28], [33]. Gly is the amino acid glycine, the smallest of the amino acids. With this repeat for each strand, a glycine amino acid is along the central

axis of the tropocollagen molecule [23], [34], [35]. This allows the three strands to orient themselves in such a way as to form stabilizing hydrogen bonds.

The combination of the alpha-1 type-1 and alpha-1 type-2 helices creates the right handed helix of the TC molecule. Additionally, a pattern exists between the X and Y position of the three amino acid subunit. Two common repetitions are Gly-Pro-Y and Gly-X-Hyp, where Pro and Hyp represent the amino acids proline and hydroxyproline, respectively [23]–[25], [30]. A common model for the TC molecule utilizes the repeating sequence Gly-Pro-Hyp, which is shown in Figure 3.

Figure 3. Triple helix of collagen with a Gly-Pro-Hyp model; colored ribbons indicate individual PPII helix, from [25].

2. Spring Model

In order to discern the stiffness of a single molecule of tropocollagen, a basic mechanic model of a helical spring was used. This model can be used because each left-handed polyproline helix of the TC molecule can be independently treated as a spring. The stabilizing hydrogen bonds and van der Waals attraction between the three helices helps to prevent buckling and to ensure that all three helices deform symmetrically. Additional protection against buckling is provided by the close packing of the TC molecules within collagen fibrils, to be discussed later. The stiffness of the TC molecule is the summation of the stiffness of the alpha-1 type-1 and alpha-1 type-2 strands. Equation 1 was used to find the spring stiffness of each helix.

$$k = \frac{F}{y} = \frac{Gd^4}{8D^3 N_A} \tag{1}$$

where k represents the spring rate, G represents the shear modulus, d represents the wire diameter, D represents the mean coil diameter, and N_A represents the number of coils.

3. Model Derivations

To determine the quantitative values for each protein helix, it was assumed that each repeating subunit is represented by Gly-Pro-Hyp. This representative subunit provides a relatively stable position for each amino acid and allows for proper cross-linking and hydrogen bonds to form between strands [25], [27], [30], [36]. Additionally, it is the presence of the amino acids proline and hydroxyproline that most greatly influence the stiffness of collagen [37]. Although in reality the combination of proline and hydroxyproline comprise only one-sixth of the amino acid content, the chemical and molecular level effects of the excess proline and hydroxyproline can be ignored since this model relies predominantly on the structure and not the molecular interactions [34]. Additionally, modeling each subunit with this sequence matches the correct bond angles and axial repeat, 10/3, for the majority of the polyproline helices [25]. Recent studies have debated the predominance of an axial repeat of 7/2 over portions of the PPII; however, the implications of this variation are more important for molecular dynamics

studies where strain energies and steric effects of the amino acid interactions are computed and analyzed [34], [35].

The wire diameter was taken to be the average spacing between residues, 0.286 nm [26], [34], [35]. The coil diameter was derived from the diameter of a TC molecule. A TC molecule is 1.5 nm in diameter, thus, a single PPII helix was assumed to have a mean coil diameter of 0.5 nm [25], [27], [28]. The number of coils was derived from a constant axial repeat of 10/3 [23], [30]. With 1000 amino acids, this yields 300 coils.

The shear modulus was the most difficult assumption to ascertain, since no data is available as to the shear modulus of a single chain amino acid helix. In order to create a valid estimate, the bond energy of the backbone of a single subunit was calculated. Within the Gly-Pro-Hyp triplet, there are six C-N bonds and three C-C bonds along the backbone. With bond energies of $5.06 \times 10^{-19} \frac{J}{bond}$ and $5.75 \times 10^{-19} \frac{J}{bond}$, respectively, the total energy of the backbone is then $4.76 \times 10^{-18} \frac{J}{subunit}$. With a subunit volume of 7.02×10^{-29} m^3, the shear stress of the backbone is computed as energy over volume, which equates to 67.9 GPa. This is close to the typical values of aluminum (70 GPa), and thus not unreasonable. The calculation above neglects all strengthening effects of cross-linking, non-backbone atoms and other atomistic considerations, but still provides a basic starting point to calculate the overall stiffness of collagen.

The resulting values computed for Equation 1 are displayed in Table 2.

Table 2. Variable values for Equation 1.

Variable	Value	Units
G	67.9	GPa
d	0.286	nm
D	0.5	nm
N_A	300	
k	0.0015	$\frac{N}{m}$

4. Model Results

The stiffness of each helix can then be found by equating Young's Modulus to spring rate.

$$E = \left(\frac{L}{A} \right) k \tag{2}$$

From the values stated in Table 2, a spring stiffness of 0.0015 $\frac{N}{m}$ was calculated from Equation 1. The length and diameter of a PPII helix are 300 nm and 0.5 nm, respectively. However, due to the helical twist shown in Figure 3, the cross-sectional diameter is defined as 0.7 nm. When the length of 300 nm and cross sectional area of 3.85 x 10^{-19} m^2 are applied to Equation 2, a stiffness of 1.18 GPa is found for each protein helix. Since each TC molecule is the sum of three helices, the stiffness of a TC molecule is 3.54 GPa.

A comparison of the results of this study with known values from both experimental data and theoretical analysis are shown in Table 3.

Table 3. Comparison of values for tropocollagen stiffness.

Stiffness [GPa]	Method	Source
3.54	Spring model	[This Study]
1.2	Property used in finite element model	[1]
2.8	Property used in finite element model	[11]
6 - 16 (Average 6)	Molecular dynamics	[38]
7	Atomistic modeling	[39]
2.4	Atomistic modeling	[40]
3	X-ray diffraction	[41]
9	Brillouin light scattering	[42]
5.1	Brillouin light scattering	[43]
3	Estimate from persistence length	[44]
0.35–12	Estimate from persistence length	[40], [45]
4.8±1	Molecular dynamics	[46]
1.4	Debye-Waller factor	[30]
(PHG)[1] 11.37	Molecular dynamics	[36]
(PPG)[2] 13.43	Molecular dynamics	[36]

[1]PHG is a Gly-Pro-Hyp model
[2]PPG is a Gly-Pro-Pro model

These results demonstrate that the helical spring model produces a valid answer for TC stiffness, thus confirming the accuracy of this method. What this model does not provide is the transverse properties or a Poisson's ratio for TC. Thus, we must assume that collagen at upper hierarchies is isotropic with a Poisson's ratio of 0.35 [1]. This relatively high Poisson's ratio is due to the presence of water, which serves as a stabilizing agent along the length of the helix [11], [33], [37].

C. NANOSCALE CONSIDERATIONS

The nanoscale model presented is a mechanical approach to a traditionally chemical or biological problem, as modeling of molecules is generally restricted to molecular dynamics or atomistic calculations. However, with an ordered helical structure constrained on all sides to prevent buckling, a simple mechanical model produces accurate results. This model neglects the mechanical properties of water bound within the helices.

III. MICROSCALE

The previous chapter defined the material properties of the elemental composite materials of bone. From those two simple constituents, a more complex hierarchy is produced. The microscale structures of the ensuing hierarchy are highly organized and highly regular structures of collagen and hydroxyapatite. In order to calculate the representative material properties of these microstructures a micromechanics model is utilized.

A. BONE FIBRIL

The fibril is the smallest of the microstructures. It is represented by a staggered array of hydroxyapatite and tropocollagen molecules. These staggered arrays are dependent on the binding and cross-linking tendencies of tropocollagen molecules.

1. Two-Dimensional Fibril Structure

The regular organization of fibrils is caused and propagated during the expansion and re-growth of fibrils, known as fibrillogenesis. When a collagen molecule is produced it has a C-terminal and N-terminal, so named for the peptides cleaved during the transition from procollagen to collagen [26], [32]. The amino acid sequence at each terminal of the TC defines a polar reference for each molecule, as each end exhibits different cross-linking tendencies. When the collagen molecules are aligned near each other the C and N ends overlap to produce an organized structure. This preferential alignment is not unique to the ends of the TC molecules; the entire length of the TC molecule contains segments of amino acids preferential to cross-linking with adjacent tropocollagen molecules [33]. These preferential segments form a collagen network with a 40 nm gap and a regular periodicity of 67 nm [29], [32], [33], [38], [47]–[50]. These gap regions are preferential to the growth of HA, allowing for the inclusion of the reinforcing particles within the fibril composite. This structure is shown in Figure 4.

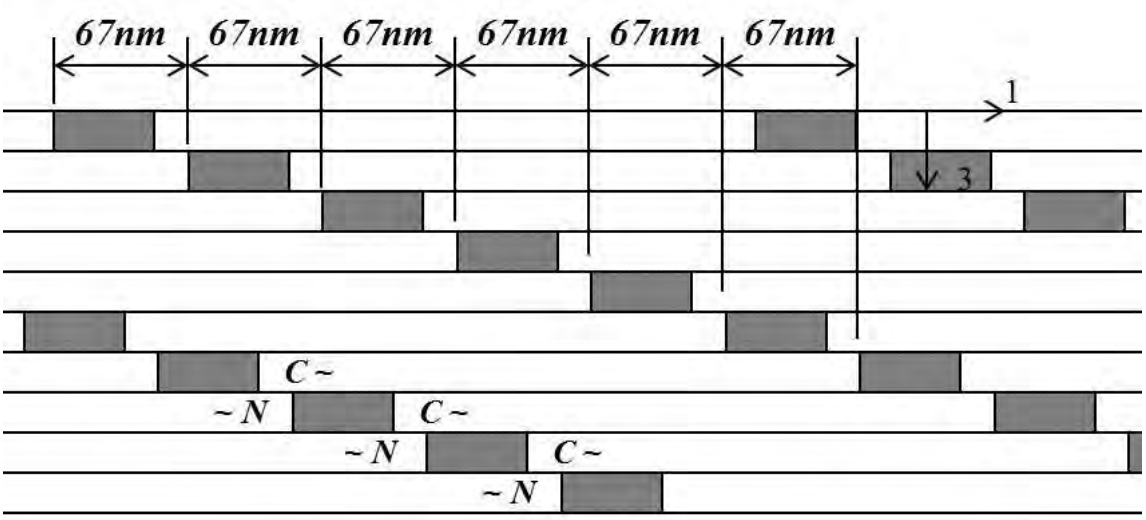

Figure 4. Visualization of 67 nm periodicity in bone fibril. Dark regions denote hydroxyapatite crystals, light regions depict tropocollagen.

Figure 4 is not to scale. The height of the crystals and TC matrix are 3 nm, while the HA crystals are 50 nm in length. This image is used to portray the periodic packing that is known to occur. This framework provides a regular structure driven by the molecular sequence of the tropocollagen molecules. Additionally, this cross-linking provides a stabilizing effect on the tropocollagen phase of the fibril [29], [37]. The presence of cross-linking prevents the individual molecules from shearing. This in turn increases strength and brittleness of the structure [11], [29]. Furthermore, the presence of cross linking allows the collagen phase to be represented as a single, continuous, material in a simplified model.

An important quality of the tropocollagen and hydroxyapatite microstructures is that the HA crystals are aligned parallel to the microfibril direction. This is due to the growth behavior of the mineral phase within the gap zones.

a. Heterogeneous Nucleation Factors

Heterogeneous nucleation factors assist in the initial deposition of HA at a molecular level [4]. An important nucleation factor is bone sialoprotein (BSP). BSP binds

directly to the ends of collagen I molecules and can be found in high concentrations within the gap zones of microfibrils [51]. BSP has been found to be a nucleator of hydroxyapatite formation, creating a HA crystal within a supersaturated medium [51].

b. Hydroxyapatite Growth

Hydroxyapatite crystals have shown preferential growth orientation related to the substrate chemistry on which they are grown [52]. Sato et al. [52] believe that the growth orientation was related to the alignment of carboxyl groups within an organic film. Chen et al. [53] further showed that the hydrothermal crystallization of hydroxyapatite can produce an oriented attachment through the use of ordered organic materials.

This process is similar to the growth of crystals in vivo. The gap zones are first supersaturated with mineral components. Then, the BSP proteins initiate crystal growth on the ends of the collagen I molecules. Subsequent crystal growth occurs in an ordered manner that aligns all crystals in parallel with the microfibril axis [51]. Since all crystals are grown in the same orientation, the stiffness values shown in Table 1 can be used as material properties for a transversely isotropic material.

One issue arises with the physical models presented based on TC cross-linking: the 40 nm gaps present in the collagen network are smaller than the 50 nm x 25 nm x 3 nm HA crystals. Researchers believe that the HA must surround the ends of the TC molecules and grow between adjacent molecules [50], [54]. This helps to prevent shearing of the HA–TC bonded surfaces. The width of the crystals represents the next challenge in modeling and determining the 3D structure of collagen fibrils.

2. Three-Dimensional Fibril Structure

The regular staggered array of a collagen fibril is easily visualized in two dimensions, however, three dimensional fibrillogenesis in vivo is still a debated topic [32], [33]. Electron micrograph images of tendon fibrils have shown different three-dimensional structures, as seen in Figure 5. Tendon fibrils are very similar in structure to bone fibrils, allowing for a feasible interpretation of HA packing models.

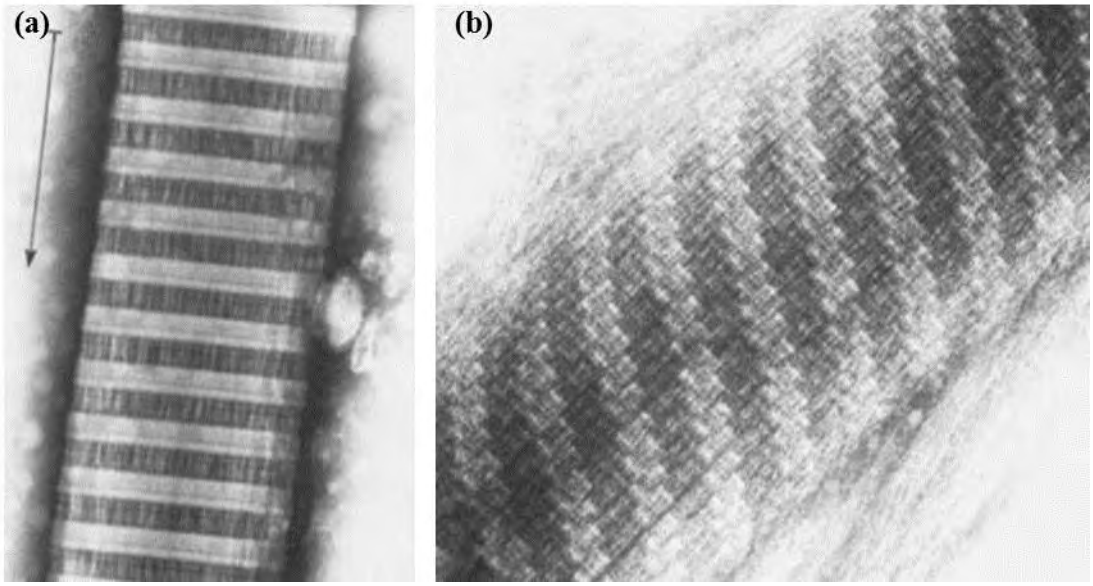

Figure 5. Electron micrograph images of 3D structures of collagen fibril, from [26]. (a) Linear crystal pattern. (b) Twisting crystal pattern.

For many years a linear fibril orientation has been the accepted model [19], [32], [33], [55], [56]. This model, shown in Figure 5a, was viewed as a long thin filament with alternating bands of mineral rich phase, sometimes referred to as the gap, and mineral deficient phase, sometimes referred to as the overlap. The mineral rich phases have approximately twice the mineral content of the mineral deficient phase [55]. Figure 6 helps visualize the three-dimensional packing of HA crystals in the linear fibril model.

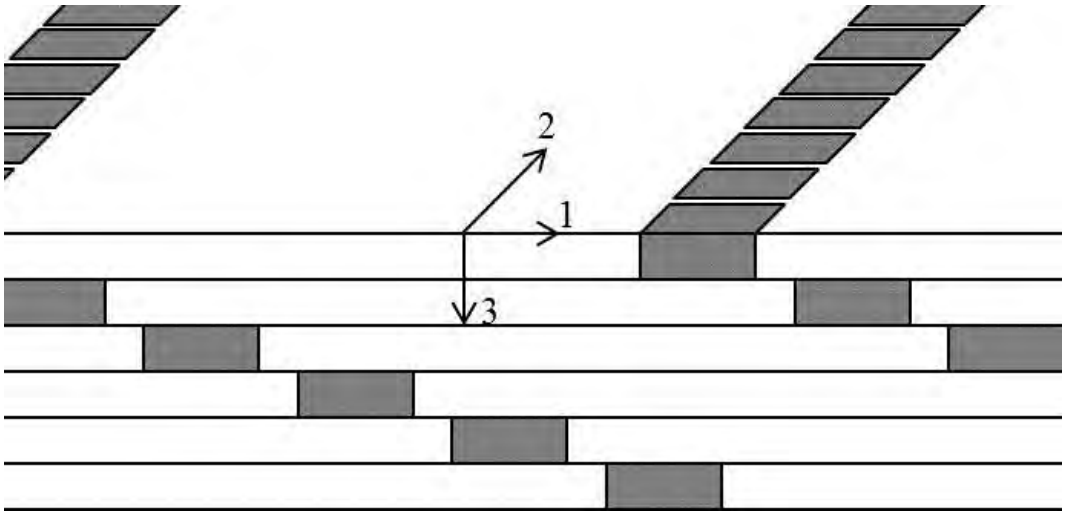

Figure 6. Simplified linear fibril model.

Although the linear model presents a viable solution to the proposed theory of three-dimensional fibrillogenesis, there has not been any evidence proving lateral growth is a purely linear process. A recent study conducted on the in vitro organization of fibril growth discovered that fibrils grow laterally in 4 nm steps [47]. Each lateral step is defined by electrostatic attraction during the formation of the microscale fibril [47]. The study, however, did not define lateral growth as it relates to longitudinal growth. A more recent model being considered is that of a twisting crystalline structure [9]. A spiral provides for a more even distribution of HA crystals. This feature is shown in Figure 5b. In the model presented, it is assumed that the 67 nm periodicity that determined the two-dimensional stacking also directs the three-dimensional pattern. For this reason, the lateral periodicity will also be 67nm. A simplified model is shown in Figure 7.

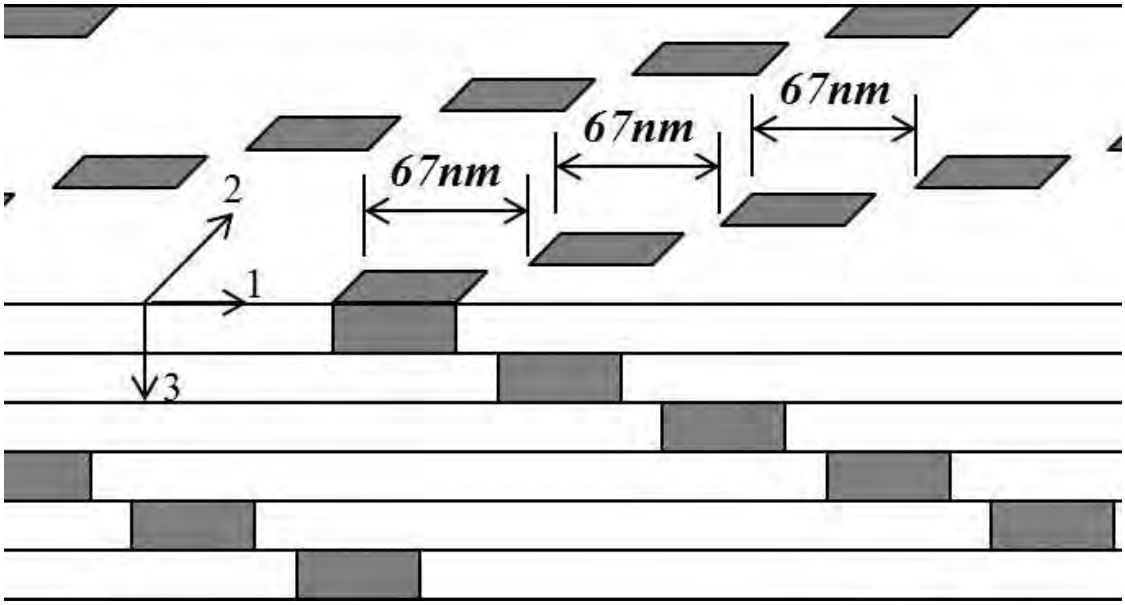

Figure 7. Twisting fibrillar model.

The two proposed fibril models shown in Figure 6 and Figure 7 are meant to help portray a simplified visualization of HA crystal distribution. The organization of bone fibril in vivo is a much more complex occurrence that includes non-collagenous proteins, errors in collagen stacking, errors in amino acid sequencing and continuous absorption and re-growth of fibrils. Moreover, biological materials are never pure substances. The collagen used in bone is only 95% collagen I [21]. Piez and Miller [26] postulate that the other collagen species help to regulate the fibrillogenesis process, but they may also introduce irregularities into the structure.

Fibrils are generally accepted to be circular, with a diameter ranging from 50 nm to 300 nm [57], [58]. It is possible, in these small diameter fibrils, that only one crystal width is present across the structure. This would validate the use of the linear fibril model. However, in larger fibrils the diameter allows for either fibril structure to be present. In order to explore the two models discussed, a micromechanical model will be modified to characterize both assemblies. The results will then be compared to experimental and theoretical data to determine validity.

3. Micromechanical Model

Kwon and Kim [59] developed a micromechanics model for the analysis of composite structures. This model is comprised of a rectangular prism divided into 8 quadrants, or subcells, shown in Figure 8.

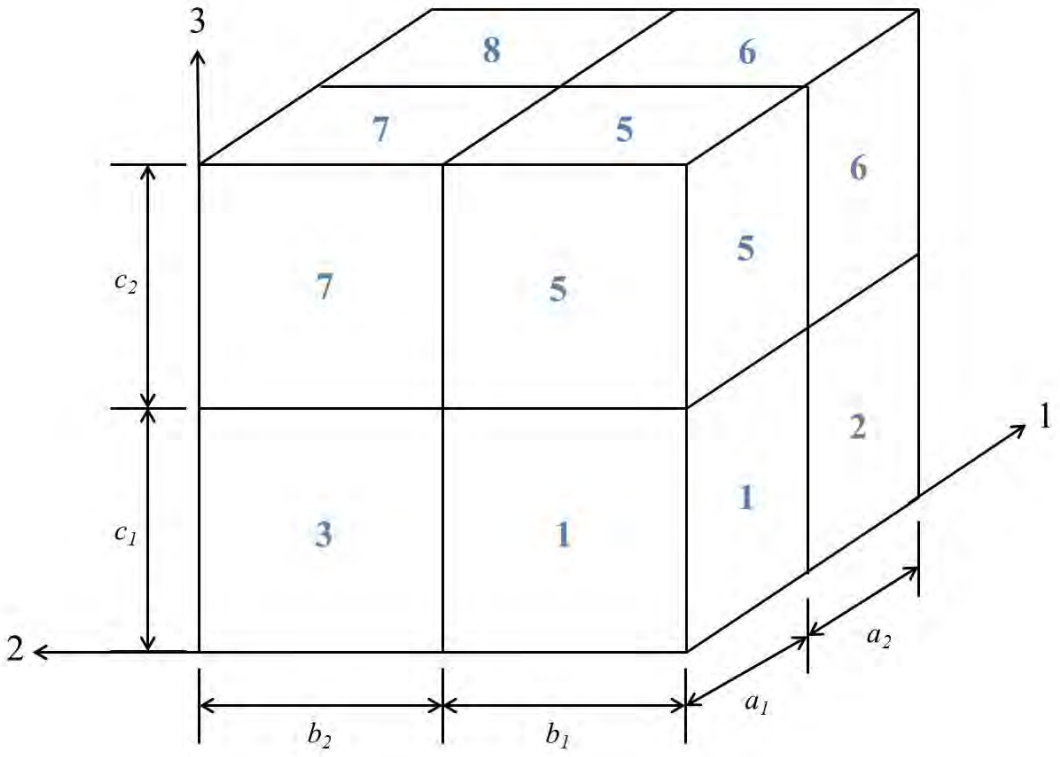

Figure 8. Unit cell of micromechanics model.

This unit cell represents a composite material, where each subcell can be identified as a different material. This model can solve for equivalent composite stiffness, rigidity, Poisson's ratio and coefficient of thermal expansion.

a. Model Derivation

In Figure 8, the numbers on the unit cell faces indicate the subcell numbers while $a-c$ indicate subcell dimensions. Additionally, each subcell is assumed to have uniform stress and strain so that the equilibrium at each interface can be defined [59]–[61]. The following equations define the equilibrium stress state at the interfaces of the subcells.

$$\sigma_{11}^1 = \sigma_{11}^2 \qquad \sigma_{11}^3 = \sigma_{11}^4 \qquad \sigma_{11}^5 = \sigma_{11}^6 \qquad \sigma_{11}^7 = \sigma_{11}^8 \tag{3a}$$

$$\sigma_{22}^1 = \sigma_{22}^3 \qquad \sigma_{22}^2 = \sigma_{22}^4 \qquad \sigma_{22}^5 = \sigma_{22}^7 \qquad \sigma_{22}^6 = \sigma_{22}^8 \tag{3b}$$

$$\sigma_{33}^1 = \sigma_{33}^5 \qquad \sigma_{33}^2 = \sigma_{33}^6 \qquad \sigma_{33}^3 = \sigma_{33}^7 \qquad \sigma_{33}^4 = \sigma_{33}^8 \tag{3c}$$

$$\sigma_{12}^1 = \sigma_{12}^2 = \sigma_{12}^3 = \sigma_{12}^4 \qquad \sigma_{12}^5 = \sigma_{12}^6 = \sigma_{12}^7 = \sigma_{12}^8 \tag{4a}$$

$$\sigma_{13}^1 = \sigma_{13}^2 = \sigma_{13}^5 = \sigma_{13}^6 \qquad \sigma_{13}^3 = \sigma_{13}^4 = \sigma_{13}^7 = \sigma_{13}^8 \tag{4b}$$

$$\sigma_{23}^1 = \sigma_{23}^3 = \sigma_{23}^5 = \sigma_{23}^7 \qquad \sigma_{23}^2 = \sigma_{23}^4 = \sigma_{23}^6 = \sigma_{23}^8 \tag{4c}$$

The subscripts denote stress components according to the axis in Figure 8 while the superscripts indicate subcell number. In addition to stress equilibrium, deformation compatibility must be met for the unit cell. Deformation compatibility defines the following set of equations.

$$a_1\varepsilon_{11}^1 + a_2\varepsilon_{11}^2 = a_1\varepsilon_{11}^3 + a_2\varepsilon_{11}^4 = a_1\varepsilon_{11}^5 + a_2\varepsilon_{11}^6 = a_1\varepsilon_{11}^7 + a_2\varepsilon_{11}^8 \tag{5a}$$

$$b_1\varepsilon_{22}^1 + b_2\varepsilon_{22}^3 = b_1\varepsilon_{22}^2 + b_2\varepsilon_{22}^4 = b_1\varepsilon_{22}^5 + b_2\varepsilon_{22}^7 = b_1\varepsilon_{22}^6 + b_2\varepsilon_{22}^8 \tag{5b}$$

$$c_1\varepsilon_{33}^1 + c_2\varepsilon_{33}^5 = c_1\varepsilon_{33}^2 + c_2\varepsilon_{33}^6 = c_1\varepsilon_{33}^3 + c_2\varepsilon_{33}^7 = c_1\varepsilon_{33}^4 + c_2\varepsilon_{33}^8 \tag{5c}$$

$$(a_1b_1)\varepsilon_{12}^1 + (a_2b_1)\varepsilon_{12}^2 + (a_1b_2)\varepsilon_{12}^3 + (a_2b_2)\varepsilon_{12}^4 = (a_1b_1)\varepsilon_{12}^5 + (a_2b_1)\varepsilon_{12}^6 + (a_1b_2)\varepsilon_{12}^7 + (a_2b_2)\varepsilon_{12}^8 \tag{6a}$$

$$(a_1c_1)\varepsilon_{13}^1 + (a_2c_1)\varepsilon_{13}^2 + (a_1c_2)\varepsilon_{13}^5 + (a_2c_2)\varepsilon_{13}^6 = (a_1c_1)\varepsilon_{13}^3 + (a_2c_1)\varepsilon_{13}^4 + (a_1c_2)\varepsilon_{13}^7 + (a_2c_2)\varepsilon_{13}^8 \tag{6b}$$

$$(b_1c_1)\varepsilon_{23}^1 + (b_2c_1)\varepsilon_{23}^3 + (b_1c_2)\varepsilon_{23}^5 + (b_2c_2)\varepsilon_{23}^7 = (b_1c_1)\varepsilon_{23}^2 + (b_2c_1)\varepsilon_{23}^4 + (b_1c_2)\varepsilon_{23}^6 + (b_2c_2)\varepsilon_{23}^8 \tag{6c}$$

Furthermore, each subcell has a constitutive equation defining strain [61].

$$\varepsilon_{ij}^n = C_{ijkl}^n\sigma_{kl}^n + \alpha_{ij}^n\Delta\theta \tag{7}$$

The superscripts represent the subcell number and subscripts represent tensor notation. C_{ijkl}^n is the stiffness tensor and α_{ij}^n is the thermal expansion tensor. For this model, the thermal expansion of the materials is ignored. This can be assumed because the internal temperature of the human body is highly regulated. This internal temperature regulation results in a negligible thermal stress component.

The volume fraction of each subcell can be calculated from the dimensions of the unit cell and represented in vector form as V^n or matrix form as $[V]$. The total unit cell stress and strain can then be found by averaging the subcell stresses and strains based on subcell volume [59]–[61].

$$\bar{\sigma}_{ij} = \sum_{n=1}^{8} V^n \sigma_{ij}^n \tag{8}$$

$$\bar{\varepsilon}_{ij} = \sum_{n=1}^{8} V^n \varepsilon_{ij}^n \tag{9}$$

The overbars in Equations 8 and 9 represent the unit cell values. With Equations 3, 5, and 9, a matrix equation can be formed for the normal properties of the composite, as shown in Equation 10.

$$[T]\{\varepsilon\} = \{f\} \tag{10}$$

$[T]$ is a 24×24 matrix with the combination of three vectors containing stress relationships, strain relationships and constitutive equations.

$$[T]^T = \left[[T1]\ [T2]\ [T3]\right]$$

$[T1]$ is a 24×12 matrix of normal stress relationships, $[T2]$ is a 24×9 matrix of normal strain relationships and $[T3]$ is a 24×3 matrix of constitutive equations. $\{f\}$ is a 24×1 column vector composed of a 21×1 column containing zeros, representing the stress and strain equilibrium, and a 3×1 column containing the effective normal strains [59].

$$\{f\}^{-1} = \left[[0]\ \left[\bar{\varepsilon}_{11}\ \ \bar{\varepsilon}_{22}\ \ \bar{\varepsilon}_{33}\right]^{-1}\right]$$

The assumption that thermal stresses are zero has greatly simplified the model from [59]. Algebraic arrangement of $[T]$ within Equation 12 produces the following relationship.

$$\{\varepsilon\} = [T]^{-1}\{f\} \tag{11}$$

The inverse of $[T]$ can be further broken down into three matrices. These can then be substituted into Equation 11 to obtain the following.

$$\begin{aligned}[T]^{-1} &= \left[[R1]\ [R2]\ [R3]\right] \\ \{\varepsilon\} &= [R3]\left[\bar{\varepsilon}_{11}\ \ \bar{\varepsilon}_{22}\ \ \bar{\varepsilon}_{33}\right]^{-1}\end{aligned} \tag{12}$$

Furthermore, Equation 8 can be written as:

$$\{\bar{\sigma}\} = [V]\{\sigma\} \tag{13}$$

With Equations 7 and 12 substituted into Equation 13, the following unit cell stress equation is found.

$$\{\bar{\sigma}\} = [V]([E]\{\varepsilon\}) = [V][E][R3]\{\bar{\varepsilon}\} \tag{14}$$

$[E]$ is a matrix of the inverse of the subcell compliance tensors stated in Equation 7. From Equation 14 the unit cell stiffness can be calculated.

$$[\bar{E}] = [V][E][R3] \tag{15}$$

The $[\bar{E}]$ matrix found through Equation 15 is the 3×3 matrix of the unit cell stiffness. With these values the Poisson's ratio of the unit cell can also be found. A similar method can be utilized to solve for the shear properties of the composite material. However, different stress relationships and deformation values are utilized. Equation 10 remains the base equation, but with a slight variation. The shear properties will be defined through Equation 16.

$$[TT]\{\varepsilon\} = \{ff\} \tag{16}$$

The $[TT]$ matrix utilized for shear properties is composed of three sub-matrices, as with normal deformation.

$$[TT]^{T} = \left[[TT1]\ [TT2]\ [TT3]\right]$$

$[TT1]$ is a 24×18 matrix of shear stress relationships, $[TT2]$ is a 24×3 matrix of shear strain relationships and $[TT3]$ is a 24×3 matrix of shear constitutive equations. $\{ff\}$ is a 24×1 column vector composed of a 21×1 column containing zeros, representing the stress and strain equilibrium, and a 3×1 column containing the effective shear strains [59].

$$\{ff\}^{-1}=\left[[0]\ \left[\bar{\gamma}_{12}\ \ \bar{\gamma}_{13}\ \ \bar{\gamma}_{23}\right]^{-1}\right]$$

Derivation of composite properties follows the process shown through Equations 11–14, however, shear calculations utilize the $[TT]$ and $\{ff\}$ matrices. The resulting equation solves for the composite shear properties.

$$\left[\bar{G}\right]=[V][G][RR3] \tag{17}$$

$\left[\bar{G}\right]$ is representative of the inverse of the compliance matrix for the composite. $[RR3]$ is derived from the inverse of the $[TT]$ matrix. This model assumes independent normal and shear properties. Modification is simple because the only inputs required are the dimensions of the unit cell and the compliance tensor of each material used. The coding of the model allows for each cell to have a different material property, if needed.

b. Subunit Quantification

For the purpose of this work, the collagen network is assumed to stagger its array with at least a 25 nm width, so as to allow for the generally accepted dimensions of the HA crystals. However, the micromechanical model will provide relevant results for both the lateral packing model and the twisted packing model mentioned above. For both models, the material properties shown in Table 4 will be used.

In addition to using two different models to explore the crystal arrays within fibrils, the presence of water will be taken into account with the calculation of material properties. The presence of water produces a bi-modulus composite material, as water is only considered in compression. While the volume percent water is much higher in

tendons and ligaments, bone is known to be approximately 10–25% water [11]. Some of this is thought to be found within the nanoscale tropocollagen and hydroxyapatite. Water serves as a binding and stabilizing agent within the triple helix of tropocollagen [33], [37]. Additionally, small amounts of water are tightly bound within the HA crystal [11]. However, the remaining water is assumed be held within the various hierarchies. For the purpose of the fibrillar model, each unit cell is assumed to have 8% volume of water. This is calculated by adjusting the stiffness of collagen to account for water in compression and void space in tension. Tropocollagen in compression and tension exhibits the different properties shown in Table 4.

Table 4. Fibril model component material properties.

Material	E_1 [GPa]	E_{23} [GPa]	ν	G [GPa]
Hydroxyapatite	150.38	143.56	0.23	59.744
Tropocollagen (compression)	3.428	3.428	0.35	1.270
Tropocollagen (tension)	3.256	3.256	0.35	1.206

(1) Linear Fibril Subunit

The linear packing model is a lateral repeat of the two-dimensional fibril array shown in Figure 4. Each crystal shown in the model has a length of 50 nm, a width of 25 nm, and a height of 3 nm. The cross section used to create a repeating subunit of the array is shown in Figure 9.

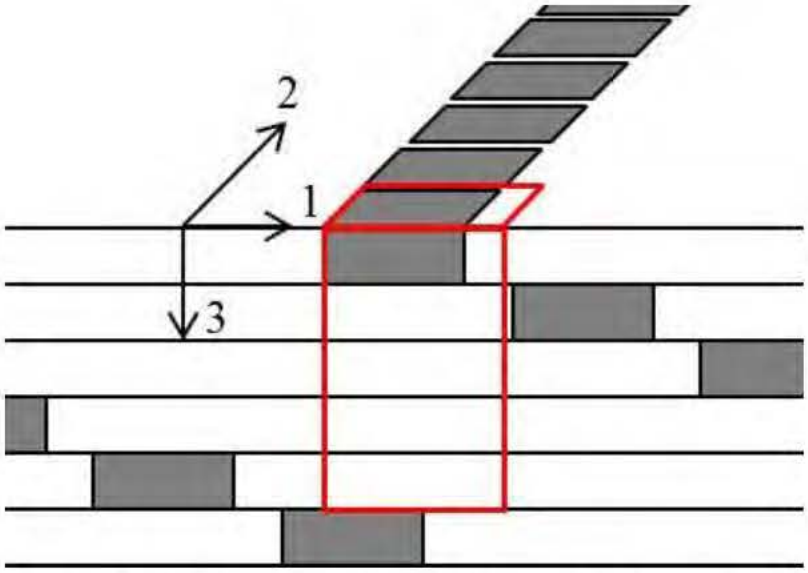

Figure 9. Subunit applied to the linear fibril model.

This small section is repeated throughout the array in 67 nm increments. The dimensions as they apply to the unit cell are listed in Table 5.

Table 5. Unit cell dimension for linear fibril model.

Dimension	Value [nm]
a_1	50
a_2	17
b_1	25
b_2	3
c_1	3
c_2	9

This model allows for the characteristic 67 nm periodicity in the 1 direction, a 3 nm buffer between each subsequent HA crystal in the 2 direction, and the vertical spacing in the 3 direction associated with the linear packing model. Subcell 1 is assigned HA properties; the remaining subcells are assigned TC properties.

(2) Twisting Fibril Subunit

The twisting fibril takes into account a 67 nm periodicity in the 2 direction as well as the 3 direction. Additionally, because each repeated stack in the 2 direction contains the same 67 nm periodicity in the 3 direction, the subunit is shortened in the 3 direction. Figure 10 shows the representative area used for the twisted fibril subunit.

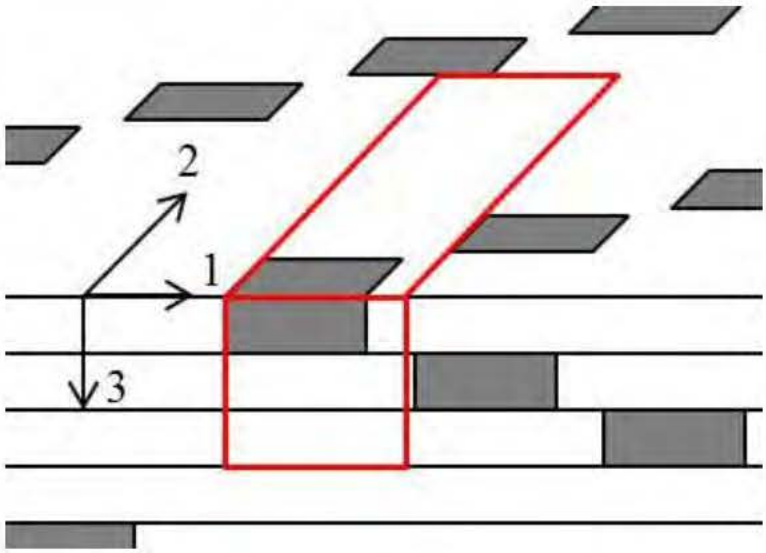

Figure 10. Subunit employed in the twisting fibril model.

The dimensions associated with the twisting model are shown in Table 6. It should be noted that the dimensions for the a_1, a_2, b_1, and c_1 lengths are restrained due to the 67 nm periodicity in the 1 direction and the known size of the HA crystals.

Table 6. Unit cell dimension for twisting fibril model.

Dimension	Value [nm]
a_1	50
a_2	17
b_1	25
b_2	75
c_1	3
c_2	6

For the twisting model, subcell 1 is assigned HA properties and the remaining subcells are assigned TC properties.

c. Model Results

The micromechanics model calculates the orthotropic properties that result from a non-symmetric unit cell. However, in vivo we can expect to find fibrils with transverse isotropic properties. This is a result of the random dispersion of radial orientations. The 1 axis lies along the fiber axis, but the 23 plane orientation will be different for each fibril. In order to convert the raw results into transverse isotropic material properties, the average of E_2 and E_3 were calculated and the average of G_{12} and G_{13} were calculated. Additionally, only two Poisson's ratios are needed; these were found by averaging ν_{21} and ν_{31} to find ν_{21}, while ν_{32} and ν_{23} were averaged to find ν_{32}. The resulting values are shown in Table 7.

Table 7. Transverse isotropic fibril results. Young's modulus and shear modulus shown in GPa.

Model		E_1	E_{23}	G_{23}	G_{12}	ν_{21}	ν_{32}
Linear	Compression	6.050	6.601	1.534	1.677	0.299	0.295
	Tension	5.760	6.298	1.458	1.593	0.299	0.295
Twisting	Compression	4.264	3.812	1.354	1.368	0.309	0.366
	Tension	4.054	3.621	1.286	1.299	0.309	0.366

These results can be compared to the experimental and theoretical values shown in Table 8. The experimental results of nanoindentation and dynamic mechanical analysis evaluate the transverse stiffness of a fibril in compression. The other results, unless noted, tested the longitudinal stiffness in tension.

Table 8. Comparison of values for fibril results.

Stiffness [GPa]	Method	Source
7.65±3.85	Nanoindentation of rat tail tendon (Transverse)	[56]
1.00±0.75	Finite element model, tension (Longitudinal)	[11]
7.5±5.5	Finite element model, compression (Longitudinal)	[11]
4.96±0.57	Dynamic mechanical analysis using AFM , peak (Transverse)[1]	[58]
3.07±0.23	Dynamic mechanical analysis using AFM, trough (Transverse)[1]	[58]
4.36	Molecular multi-scale modeling (small strain)	[29]
38	Molecular multi-scale modeling (large strain)	[29]
10±2.0	3D molecular dynamics (Longitudinal)	[48]
5	Molecular modeling (Longitudinal)	[50]
4.81	Molecular dynamics and finite element modeling (Longitudinal)	[54]
2.05±0.75	Full atomistic model (Longitudinal)	[19]
4.75±3.06	Finite element model (Longitudinal)	[55]

[1]Peak and trough refer to mineralized and un-mineralized sections, respectively.

As the results shown in Table 8 confirm, the micromechanics model utilized for bone fibrils is within the range of values defined for bone fibrils. The model provides a simple solution to a complex problem. The relatively elementary approach yielded realistic results for both the linear fibril model and the twisting fibril model. Additionally, the micromechanics model calculated the Poisson's ratios for the fibril rather than assuming a value, as did all results in Table 8.

4. Fibril Discussion

The micromechanics model produces accurate results for the stiffness of bone fibrils in tension and compression. The calculation of transverse isotropic material properties, to include Poisson's ratios and shear moduli, can be used to increase the accuracy of subsequent hierarchies, as the micromechanics model will be used once again for the calculation of fiber properties.

One metric for comparing validity of theoretical models is to compare bone mineral content. However, very little information is available as to the mineral content of

microstructures. Therefore, the mineral content at each level will be tracked for comparison at the macro level. Table 9 displays the mineral content of the two fibril models proposed.

Table 9. Fibril model mineral volume fraction.

Model	Mineral Volume Fraction [%]
Linear	16.66
Twisting	6.22

B. BONE FIBER

The successive hierarchy following the bone fibril is that of the bone fiber. Fibers are a composite material of fibrils and HA. The HA is present in the fibers in the form of extrafibrillar mineral, deposited between densely packed fibrils [2], [9], [14], [62].

1. Fiber Structure

Bone fibers are sometimes referred to as fibril bundles. After fibrils have been arranged in their three-dimensional space, mineral is deposited on the outside of the fibril. This extrafibrillar mineral acts as a stiffener for the bundles. These mineralized fibrils are tightly packed in a uniform direction [9], similar to a fiber reinforced composite [7]. This grouping of fibrils creates the fiber structure. The mineralization of fibrils is shown in Figure 11.

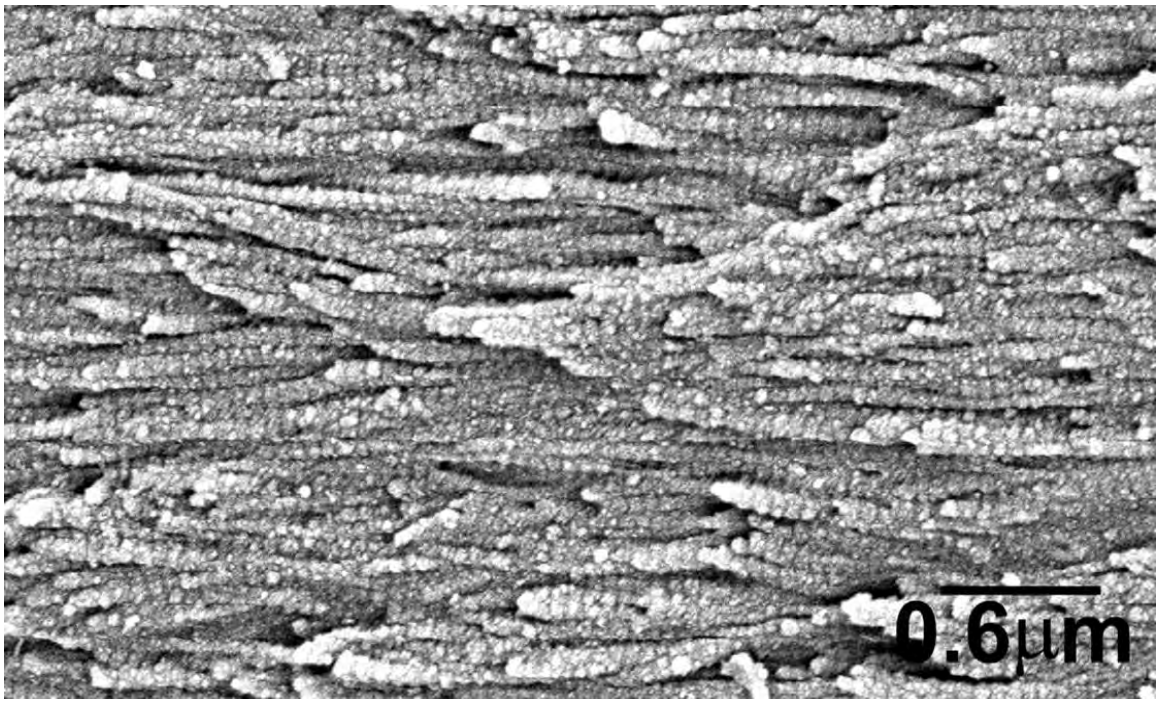

Figure 11. Scanning electron micrograph of a mineralized fibril, from [63].

a. Three-Dimensional Fiber Structure

Each closely packed fibril is surrounded by a crust of mineral, approximately 20–30 nm thick [7], [62]. The HA is grown as small plates that combine to coat the fibrils [7], [9]. This provides an ordered arrangement of minerals, where the 1 axis of minerals and fibrils run parallel to each other [19], [62], [63]. This allows us to represent HA as a transversely isotropic material. The thickness of the crust will be estimated as 26 nm. Additionally, a single uniform fibril diameter of 150 nm will be assumed [7], [9]. This three-dimensional structure is shown in Figure 12, with the surface mineral removed.

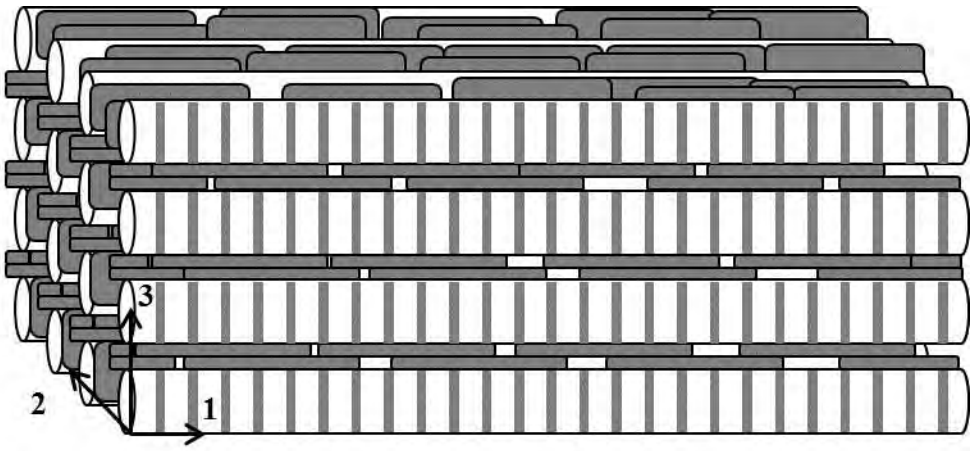

Figure 12. Three-dimensional fiber array. Dark rectangles represent HA crystals while the rod structures represent fibrils.

The fibrils of Figure 12 exhibit a linear crystal pattern, however, both linear and twisting mineral patterns will be analyzed. Very little is known about the degree of mineralization along the lengths of the fibrils [3], [9]. In order to analyze the effects of extrafibrillar mineralization (EFM), several degrees of mineralization will be tested.

b. Inclusion of Non-structural Materials

Mineral packing at the fiber level is not a close-packed assembly, as Figure 12 shows. The minerals allow for void spaces between them. These voids at the micro level allow for the presence of water with dissolved non-structural proteins and macromolecules [9]. This solution is often referred to as the extrafibrillar matrix. This liquid phase at the fiber level represents the remaining component of bone water [11] These spaces will be treated as water, resulting in a bi-modulus property for fibers.

2. Micromechanical Fiber Model

The fibers found in the macro level are single bundles of fibrils or a combination of many bundles. The bundles are an organized and repeating arrangement of fibrils and HA. Accordingly, the micromechanics model is aptly suited for modeling bone fiber. The fiber model will not rely on exact dimensions, as did the unit cell for the fibril models. The fiber unit cells will rely on volume fractions of each material. In order to ensure a volume of unity, Equation 18 will be adhered to.

$$a_1 + a_2 = b_1 + b_2 = c_1 + c_2 = 1 \tag{18}$$

Additionally, since all fibrils are assumed circular, symmetry can be applied. This allows a mineralized fibril to be split into four equal quadrants.

a. Unit Cell Dimensions

For all models, the longitudinal cross section will remain constant, as derived from the area percent HA on the 1 face. This area percent assumes a total crust thickness of 26 nm and a fibril diameter of 150 nm. When symmetry is applied, a crust of 13 nm and a radius of 75 nm are utilized. In order to apply this to the micromechanics model, the dimensions shown in Table 10 will be applied to the 1 face.

Table 10. Fiber unit cell 1 face dimension.

Dimension	Value
b_1	85
b_2	15
c_1	85
c_2	15

This equates to a fibril area of 72.25% when converted into the micromechanics model. This is visualized in Figure 13.

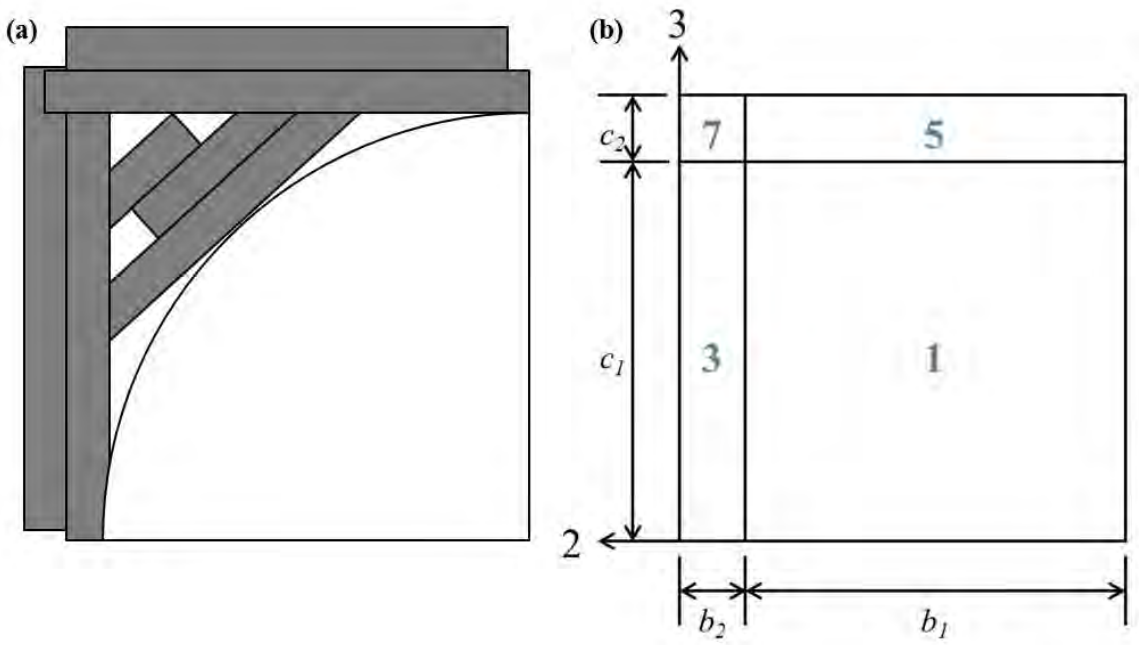

Figure 13. Longitudinal fiber cross section as compared to micromechanics model cross section. (a) Fiber cross section: dark area represents mineral, light section represents fibril. (b) Micromechanics model longitudinal cross section.

Subcell 1 represents the fibril. In order to test the effect of fibril mineralization, the degree of mineralization will be varied. %EFM will be defined as the total percent of fibril covered by mineral and is equal to the volume of subcells 3, 5, and 7, shown in Figure 14.

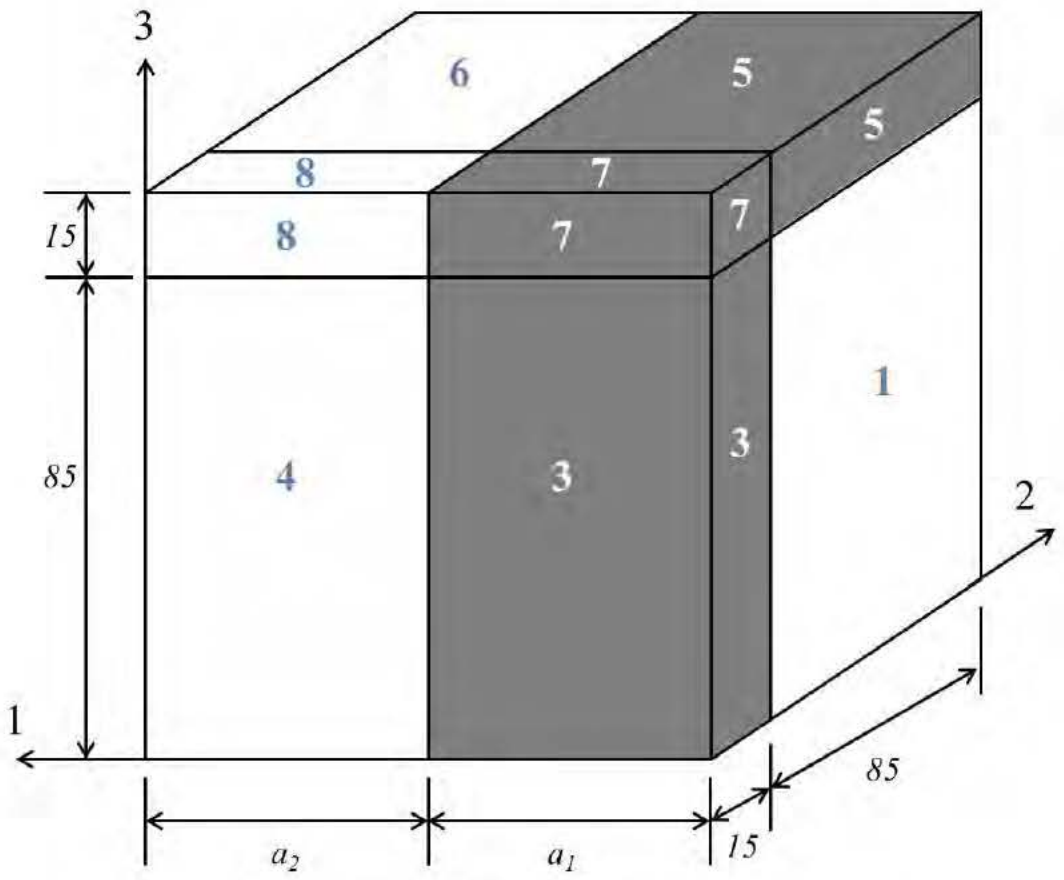

Figure 14. Unit cell for fiber micromechanics model.

By altering the length of a_1, %EFM is modified for the fiber. We will assume that the fiber is comprised of no more than 95% EFM. The different levels of mineralization analyzed are listed in Table 11.

Table 11. Fiber unit cell extrafibrillar mineralization dimensions.

%EFM	a_1	a_2
50	50	50
70	70	30
90	90	10
95	95	5

In addition to altering the %EFM of the unit cell, the effects of water will be taken into account. In compression, subcells 4, 6, and 8 will be assigned the properties of water. In tension, these subcells will be assigned as void spaces. In order to apply stiffness and Poisson's ratio to water, it was assumed to be slightly compressible. Additionally, the elastic modulus was assumed equal to the bulk modulus when confined to small constrained volumes, as with microscale bone. Therefore, the Poisson's ratio can be solved using Equation 19.

$$\nu = \frac{3K - E}{6K} = \frac{3K - K}{6K} = \frac{2K}{6K} = \frac{1}{3} \tag{19}$$

where K is the bulk modulus. The material properties for water and void space are listed in Table 12. The material properties for HA and the fibril are listed in Table 4 and Table 7, respectively.

Table 12. Material properties of water and void space.

Material	E [GPa]	ν	G [GPa]
Water	2.15	0.33	0.001
Void	0.001	0. 001	0.001

b. Results

The results for the fiber model were calculated both in compression and tension. As expected, due to the applied symmetry, the fiber exhibits transverse isotropic material properties. This is due to the assumption that the radial arrangement of the fiber arrays is a random occurrence. The results from the fiber models are split into two tables for easier comparison. Table 13 shows the results in compression, while Table 14 shows the results in tension.

Table 13. Fiber results in compression.

	50% EFM		70% EFM		90% EFM		95% EFM	
	Linear	Twisting	Linear	Twisting	Linear	Twisting	Linear	Twisting
E_1 [GPa]	6.511	5.446	7.567	6.509	11.60	10.47	16.17	14.97
E_{23} [GPa]	16.66	14.62	21.41	19.16	26.35	23.91	27.72	25.23
G_{23} [GPa]	1.053	0.931	1.473	1.302	1.893	1.672	1.998	1.765
G_{12} [GPa]	0.012	0.012	0.019	0.019	0.056	0.056	0.109	0.108
ν_{21}	0.369	0.413	0.364	0.397	0.295	0.307	0.245	0.250
ν_{32}	0.140	0.132	0.128	0.119	0.126	0.118	0.127	0.120

The results in compression show that the linear fibril model produces a stiffer fiber in all normal and shear cases and in all directions. For all %EFM the fiber shear modulus in the 12 direction is much less than the 23 direction. As %EFM increases from 50% to 95%, the 12 shear modulus increases by an order of magnitude, while the 23 modulus approximately doubles. This is shown for both the linear and the twisting models. The Poisson's ratio in the 32 direction remains relatively constant, but as %EFM increases the Poisson's ratio in the 21 direction decreases.

Table 14. Fiber results in tension.

	50% EFM		70% EFM		90% EFM		95% EFM	
	Linear	Twisting	Linear	Twisting	Linear	Twisting	Linear	Twisting
E_1 [GPa]	4.527	3.374	4.691	3.592	4.870	3.841	4.919	3.911
E_{23} [GPa]	14.10	12.80	19.74	17.95	25.38	23.03	26.79	24.31
G_{23} [GPa]	1.001	0.885	1.401	1.237	1.800	1.589	1.900	1.677
G_{12} [GPa]	0.012	0.012	0.019	0.019	0.056	0.056	0.109	0.107
ν_{21}	0.227	0.266	0.318	0.372	0.408	0.478	0.431	0.505
ν_{32}	0.113	0.099	0.113	0.099	0.113	0.099	0.113	0.099

The results in tension show similar results to those in compression. The linear model exhibits greater stiffness for all results. Additionally, the values of E_{23} are much

greater than E_1. The value of ν_{32} remains constant for each model as %EFM increases. However, the value of ν_{21} increases steadily as %EFM increases.

3. Fiber Results Discussion

The shear moduli in the 12 direction are very low for small %EFM. This is due to the void relatively large amount of void space present within the unit cell. However, this will be redressed with structure of lamellar bone. The inclusion of fibers within the disordered fibrillar matrix will increase the shear modulus in the 12 direction.

The difficulty with evaluating the results of the fiber model is that there is an absence of experimental testing available for comparison. Fibers exist within the macrostructures of bone and are not easily isolated for testing. Additionally, almost all theoretical calculations assume that macrostructure bone is composed solely of layered fibers. Due to the recent findings of [12], we know this not to be true. The macrostructures of bone are a fiber reinforced composite with fibrils acting as the matrix and bone fibers as the fibers.

The mineral content completely surrounds the fibril. This complete encirclement increases the normal stiffness in the 23 direction and stiffens the fiber against shear on the 23 plane. The mineral content of the different fiber models was calculated. These calculations include both intrafibrillar and extrafibrillar HA. The resulting values are shown in Table 15.

Table 15. Fiber model mineral volume fraction.

	Mineral Volume Fraction [%]	
%EFM	Linear	Twisting
50	25.91	18.37
70	31.46	23.92
90	37.01	29.47
95	38.40	30.86

C. MICROSCALE CONSIDERATIONS

The models presented for the microscale components of bone provide simple and accurate solutions. They calculate transverse isotropic material properties driven by the ordered geometry inherent to the self-assembly of living materials. However, not everything is known about the microstructures of bone.

1. Biological Unknowns

There is very little information as to the effective length of microstructures. It is difficult to produce an image detailing the beginning and end of fibrils or fibers [62]. In addition to not knowing the length of these structures, little information is known about the attachment of these endpoints or how they are secured within the surrounding material. The concept of twisting HA crystals in fibrils is a recent proposition [9]. As Figure 5b shows, the lateral spacing is not restricted to a 67 nm periodicity. With no definitive model of three-dimensional fibril packing, the linear fibril model presents the most biologically probable result.

The micromechanics model developed relies on selecting the proper unit cell dimensions. With the linear model, the dimensions presented are logically derived. The twisting model is based on the theoretical assumption that an incorporated twist is a natural occurrence. This introduces two unknowns that need to be addressed. The rate of twist is undefined and the twist is not restricted to lateral packing, but to the surface of a fibril with a circular cross section. Thus, the models presented in this study assumed a lateral packing with a periodicity of 67nm. This introduces a twist in the HA crystal pattern. Due to these assumptions the unit cell dimensions are less quantitatively defined for the twisting fibril model.

Furthermore, the effect of shearing between fibrils and fibers is a currently researched topic. Several finite element models and molecular dynamics models have attempted to explain these occurrences through the use of bonding between different phases [7], [54] and energy dissipation of cross-links [29], [50]. However, no agreed upon mechanisms have been produced through these computationally expensive finite element methods (FEM) and molecular dynamics models.

These models hypothesize the chemical nature of in vivo bone at the nano and micro level. This information is difficult to obtain through laboratory testing. The challenge is understandable, as recreating the in vivo conditions in a laboratory are extremely difficult. In addition, the living cells present in micro structures provide continuous growth and remodeling of bone structures. These living cells provide another unknown variable to the modeling of bone structures.

Where information is lacking, assumptions allow results to be obtained. The models presented here help to make simple assumptions that allow for the lack of detailed information to be negated. As a result, the models match current hypotheses on the structure of microscale bone components.

2. Mineral Content

An important metric for evaluating bone is the mineral content. Studies have been completed comparing volume percent and weight percent of HA present in different structures of bone. However, many of these studies are at the macro level. A comparison will be made, once the macro level models are complete, of the various levels of mineralization.

3. Variations in Experimental Testing

As Table 8 shows, the experimental and theoretical results for biological materials are widely varied. Variations in theoretical results are due to the assumptions made at each level, the scope of the testing, the source of material properties, the complexity of each model, etc. Variations in experimental results are due to the conditions of experimental tests and the methods used for each experimental test. Experimental results test hydrated structures, dehydrated structures, structures in vitro, in vivo structures prepared in a series of solutions, non-human bone structures and many other variations. With so many variations, how is it possible to select the most accurate result?

It is for this reason that the linear and twisting fibrillar models were both used in the fiber model. It is the same reason that multiple fiber models will be applied to the macro level models. These results can then be compared to experimental results of human

bone. The results of macro scale bone are more easily standardized and tested, leading to more uniform experimental results. Additionally, once the macro scale models are compared to experimental results, the accuracy of each microscale model can be retroactively verified.

IV. MACROSCALE

From the basic building blocks of HA and TC, complex microscale geometries have been created. These microscale components serve as the elementary materials for further biocomposite materials. In order to analyze the macroscale structures of bone, three different models will be utilized: a micromechanics model of lamellar bone, a layered fiber reinforced composite model of cortical and trabecular bone, and a finite element model of a tetrakaidecahedron modeling cancellous bone.

A. LAMELLAR BONE

The next hierarchical step of bone is that of lamellar bone. Lamellar bone is a fiber reinforced composite of bone fibers and bone fibrils. The presence of a disordered fibril matrix is a relatively new discovery, identified through the use of a serial surface view (SSV). By continuously etching and imaging a section of material, the three dimensional structure is revealed. Reznikov et al. [12] has utilized SSV to three dimensionally deconstruct sections of bone.

1. Lamellar Structure

Lamellar bone is comprised of bone fibers surrounded by a matrix of disordered fibrils [9], [12]. This is a new revelation that many older models do not take into account. Previous calculations have assumed that lamellar layers are merely an ordered array of fibers [1], [3], [10], [13], [64]. The discovery of the disordered fibril matrix adds another hierarchical level that can be modeled using the micromechanics model. Reznikov et al. [12] found that the lamellar bone exhibits an ordered motif of 2-3 μm, representing the layer thickness, and disordered matrix thickness of 0.25 μm to 1 μm, representing the fibrillar matrix. In addition to the presence of a disordered matrix, the SSV discovered the presence of small pores with a diameter of 50 nm [12]. These pores are represented as voids in the lamellar matrix, to be ignored in this model. The simplified view of a single lamellar layer is shown in Figure 15.

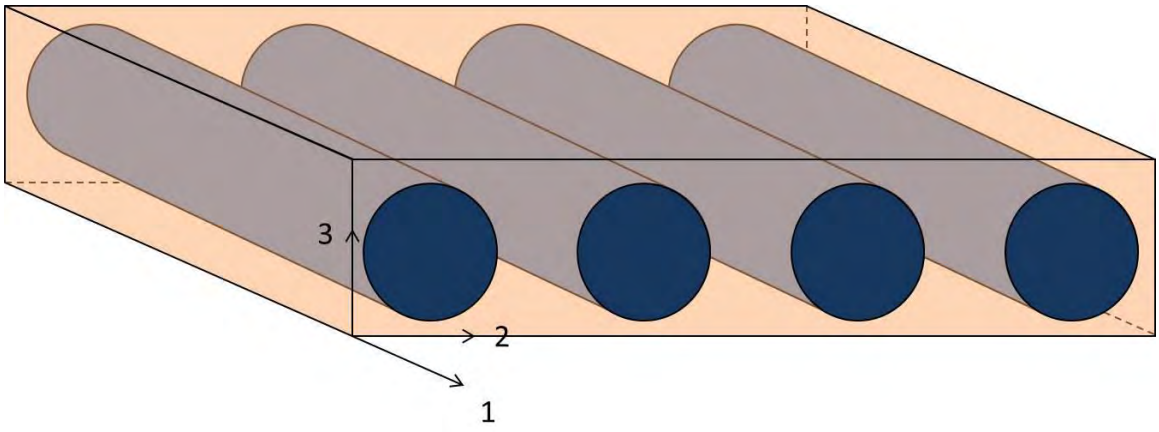

Figure 15. Single lamellar bone layer.

Although still measured in microns, the lamellar layer is quantified in the macroscale section due to the fact that it is the main constituent of cortical and cancellous bone.

2. Lamellar Layer Micromechanics Model

The calculation of material properties for lamellar bone will closely mirror the process used for analyzing the material properties of bone fibers. Utilizing the knowledge that fibers within a lamellar layer are unidirectional and that the disordered matrix has a relatively random thickness, within the bounds defined by [12], symmetry can be applied to solve for transverse isotropic material properties. The subunit to be used for the lamellar layers will assume that the layer thickness is 2.5 μm and the matrix thickness is 0.375 μm. These are the average of the range defined by [12]. The fiber diameter is then calculated to be 1.75 μm. The longitudinal cross section to be used for lamellar calculations is shown in Figure 16.

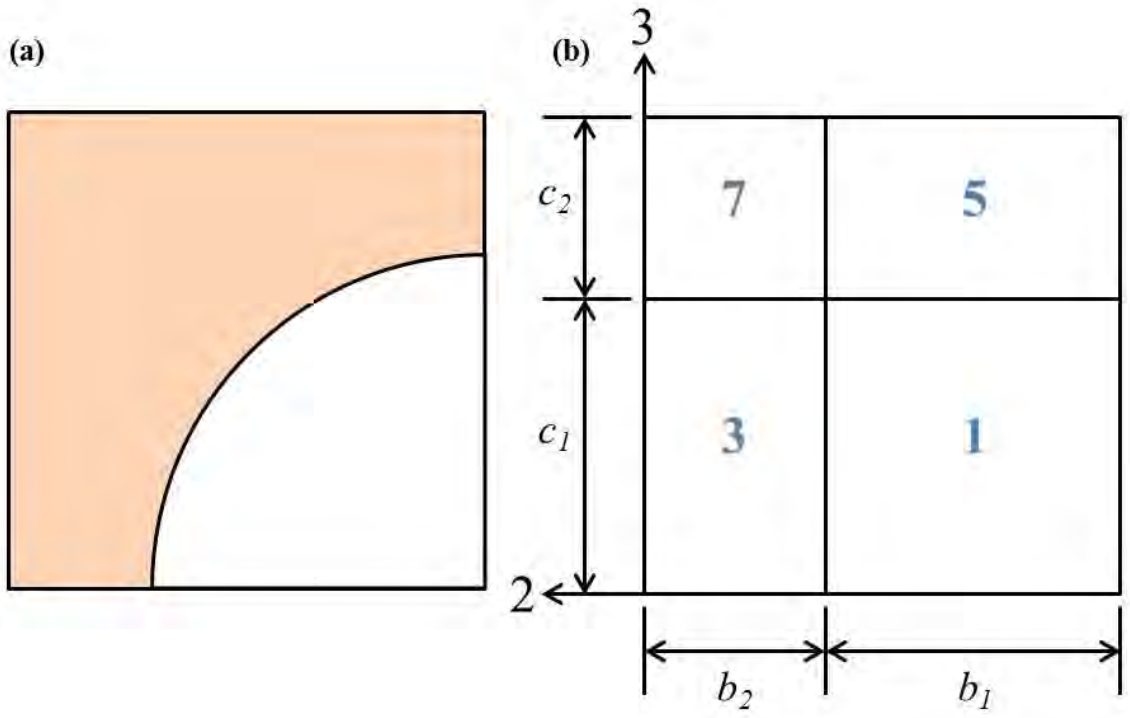

Figure 16. Longitudinal lamellar cross section as compared to micromechanics model cross section. (a) Lamellar cross section: shaded area represents disordered matrix, light section represents fiber. (b) Micromechanics model longitudinal cross section.

The longitudinal cross section of the micromechanics model, shown in Figure 16b, provides a 38.4% fiber volume for the lamellar unit cell. This is derived from the assumed fiber diameter and matrix thickness between fibers. The presence of the small pores will be neglected as they account for approximately 0.1% of the current model's volume and are not uniformly present along the length of the fibers.

The micromechanics model will once again utilize volume percent to analyze the lamellar layer; unit cell dimensions will be constrained to Equation 18. In order to model the lamellar layer as a continuous fiber, the unit cell shown in Figure 17 is used.

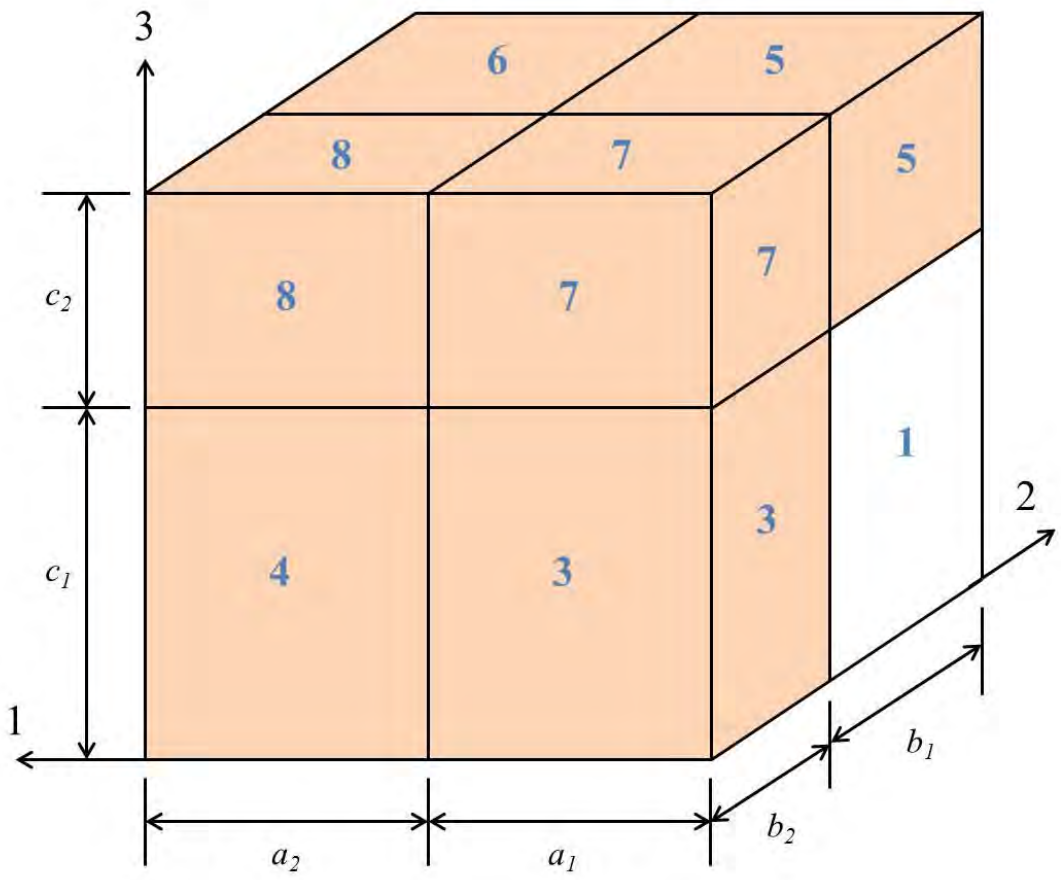

Figure 17. Unit cell for lamellar micromechanics model.

The material properties assigned to subcells 1, 3, 5 and 7 are mirrored for subcells 2, 4, 6 and 8. This produces a continuous fiber reinforced composite.

a. Unit Cell Quantification

The dimensions of a_1 and a_2 are unimportant, as the properties of the odd subcells are mirrored by the even subcells. The dimensions to be used for this model are listed in Table 16.

Table 16. Unit cell dimension for lamellar model.

Dimension	Value
a_1	50
a_2	50
b_1	62
b_2	38
c_1	62
c_2	38

The composite matrix is composed of a disordered array of fibrils. The fibrils do not exhibit any preferential alignment [12], therefore the material can be assumed isotropic. This will be accomplished by averaging the stiffnesses and Poisson's ratios found in Table 7. Furthermore, fiber models of varying %EFM will be used. Due to the bi-modulus property of the materials within the model and the applied symmetry of the unit cell, the lamellar layer is expected to show transverse isotropic, bi-modulus, material properties.

b. Results

The results of the lamellar micromechanics model were calculated in both compression and tension for four different %EFM. The resulting stiffnesses and Poisson's ratios are shown in Table 17 and Table 18.

Table 17. Lamellar results in compression.

	50% EFM		70% EFM		90% EFM		95% EFM	
	Linear	Twisting	Linear	Twisting	Linear	Twisting	Linear	Twisting
E_1 [GPa]	6.428	4.609	6.841	5.024	8.391	6.547	10.14	8.272
E_{23} [GPa]	9.001	6.425	9.717	6.928	10.35	7.409	10.55	7.576
G_{23} [GPa]	1.336	1.156	1.552	1.338	1.705	1.466	1.737	1.492
G_{12} [GPa]	0.622	0.529	0.629	0.536	0.665	0.572	0.715	0.620
ν_{21}	0.328	0.366	0.322	0.350	0.280	0.286	0.242	0.237
ν_{32}	0.237	0.266	0.235	0.269	0.243	0.288	0.252	0.302

The results of Table 17 show that the linear model exhibits greater stiffness than the twisting model for all instances. Additionally, for low %EFM the Young's modulus in the 1 direction is smaller than in the 23 direction. As %EFM increases, the two values converge. For the twisting model, the stiffness in the 1 direction surpasses the stiffness in the 23 direction.

Table 18. Lamellar results in tension.

	50% EFM		70% EFM		90% EFM		95% EFM	
	Linear	Twisting	Linear	Twisting	Linear	Twisting	Linear	Twisting
E_1 [GPa]	5.514	3.718	5.578	3.801	5.646	3.895	5.665	3.922
E_{23} [GPa]	8.305	5.992	9.174	6.538	9.781	6.902	9.905	6.976
G_{23} [GPa]	1.270	1.098	1.475	1.271	1.621	1.393	1.651	1.418
G_{12} [GPa]	0.592	0.503	0.599	0.510	0.635	0.546	0.684	0.593
ν_{21}	0.312	0.370	0.338	0.394	0.355	0.407	0.359	0.410
ν_{32}	0.235	0.262	0.230	0.257	0.226	0.254	0.225	0.253

The results in tension also show that the linear model provides greater stiffness than all twisting models. Additionally, the stiffness in the 23 direction is larger than the stiffness in the 1 direction for all %EFM.

3. Lamellar Discussion

As with microscale hierarchies, the mineral content of the lamellar layers was analyzed. The mineral volume fraction of each model is displayed in Table 19.

Table 19. Lamellar model mineral volume fraction.

	Mineral Volume Fraction [%]	
%EFM	Linear	Twisting
50	20.22	10.89
70	22.35	13.02
90	24.48	15.16
95	25.02	15.69

The mineral volume fraction within lamellar layers is representative of macroscale bone mineral content. Comparisons can be made to theoretical and experimental values. Early studies have hypothesized on the mineral content of bone through both estimations of spatial arrangement and calculation from bone ash content. Early understandings of fibril organization place total bone mineral volume content at 50% [65]. Calculation of the bone ash content of adult cows was found to be close to 70% [66]. The volume percent of bone ash does not correlate to bone mineral content. Bone ash is determined by burning a sample of bone in a furnace and comparing the ash weight. This method results in a large estimate of mineral content as additional residues remain from sources other than hydroxyapatite. More recent studies estimate a lower bone mineral volume. Kotha and Guzelsu [67] postulate that mineral volume content is 40% for bone while [68] approximates 33-43% apatite mineral volume. These estimates are based on a more complete understanding of the hierarchical structure of bone, but are still estimates as bone mineral content varies with bone type, anatomical position, age, and gender.

Comparing the bone mineral content results of this study to those found through experimental and theoretical methods, the linear crystal pattern emerges as the more viable model. The mineral volume fractions of the twisting model are too low to validate its use. Even with slight perturbations to the constraints applied to the fibril and fiber models, the mineral content of the twisting model does not match the current estimates. Future calculations will assume the linear model to be the valid model.

B. CORTICAL BONE

Cortical bone is the dense structure of macroscale bone [6]. It provides an external shell surrounding the spongy center of cancellous bone and accounts for a large percent of the weight fraction of the skeletal system. Cortical bone is composed of concentric layers of lamellar bone, known as osteons. Osteons can be made of primary or secondary bone. Primary bone is found where bone has been grown de novo. Secondary bone is created when the primary bone is broken down and re-grown in place [9]. Secondary osteons are called Haversian systems, which will be analyzed in this study.

1. Three Dimensional Haversian System Structure

The concentric layers composing Haversian systems form a cylindrical structure approximately 200 microns in diameter [9], [12], [64], [69]. At the center of these cylinders is a Haversian canal. These canals contain the blood supply and nerve endings for the surrounding bone. The canals are approximately 30-50 microns in diameter [9], [12], [64], [69].

Each concentric layer associated with the osteon is composed of lamellar bone. The fibers of each individual layer are unidirectional in alignment [9], [12], [64], [69]. The center cylinder is representative of a Haversian canal and will be represented as un-bound water [9]. Multiple Haversian systems are packed together in cortical bone. Due to their circular shape, there are incomplete layers at the interface of each Haversian system where the boundaries intersect. These boundaries are defined by a cement line, which is an identifiable region where osteon growth direction has transitioned. The properties of cement lines are similar to those of the surrounding bone, despite the misnomer of "cement" [70].

The long axis of a Haversian system is preferentially aligned with the long axis of the bone for a majority of cortical bone [64]. Transversely oriented Haversian canals do exist that interconnect each longitudinal Haversian canal, but they are very short compared to the longitudinal canals. This study will assume all Haversian systems are aligned parallel to the long axis of the bone. Additionally, as the osteoclasts and osteoblasts perform the resorption and deposition process they leave behind a small network of voids. These voids are known as canaliculi and promote the metabolic function of bone by transporting proteins and molecules within the densely packed osteons [71].

The fiber directions of the concentric lamellar layers vary for each layer. Two distinct patterns have been identified in lamellar bone: a periodic alternating pattern and a continuous fiber twist. The alternating pattern was found by both [12] and [64]. Reznikov et al. [12] utilize SSV, while Varge et al. [64] used synchrotron X-ray phase nano-tomography (SR-PNT). SR-PNT works by taking different tomographic images at periodic distances within a sample. Both sources identified a distinct alternating pattern of high and low angle fibers. This motif exhibits a layer of fibers at 65-80° and a layer at 15-30°. Reznikov et al. [12] refers to these as transverse and longitudinal orientations, respectively. Additionally, due to the imperfect nature of biomaterials, an additional percent of intermediate angles were found. The average orientations of three samples were calculated. The samples were taken from a 20 year-old female, a 59 year-old male, and a 77 year-old male. The results revealed 45% transverse fibers, 35% longitudinal fibers and 20% intermediate fibers [12]. The findings of [64] also describe a section of femur exhibiting a continuous twist of fibers from 0-180° between lamellar layers. This continuous twist changes by approximately 10° each layer. Both the periodic alternating pattern and the continuous twist can be modeled as a composite of laminated transverse isotropic plates.

2. Layered Composite Model

The layered composite of macroscale bone is composed of concentric layers of lamellar bone. The previous section derived the properties for a single layer. Two layered motifs will be analyzed with respect to cortical bone.

a. Cortical Bone Model Derivation

The stratified lamellar layers of cortical bone represent a combination of laminated plates. Each plate is represented as a transverse isotropic material. Due to the close packing of the lamellar layers within Haversian systems, the material properties of the composite can be found by analyzing each fiber orientation. The breakdown of an osteon into its respective layers can be seen in Figure 18.

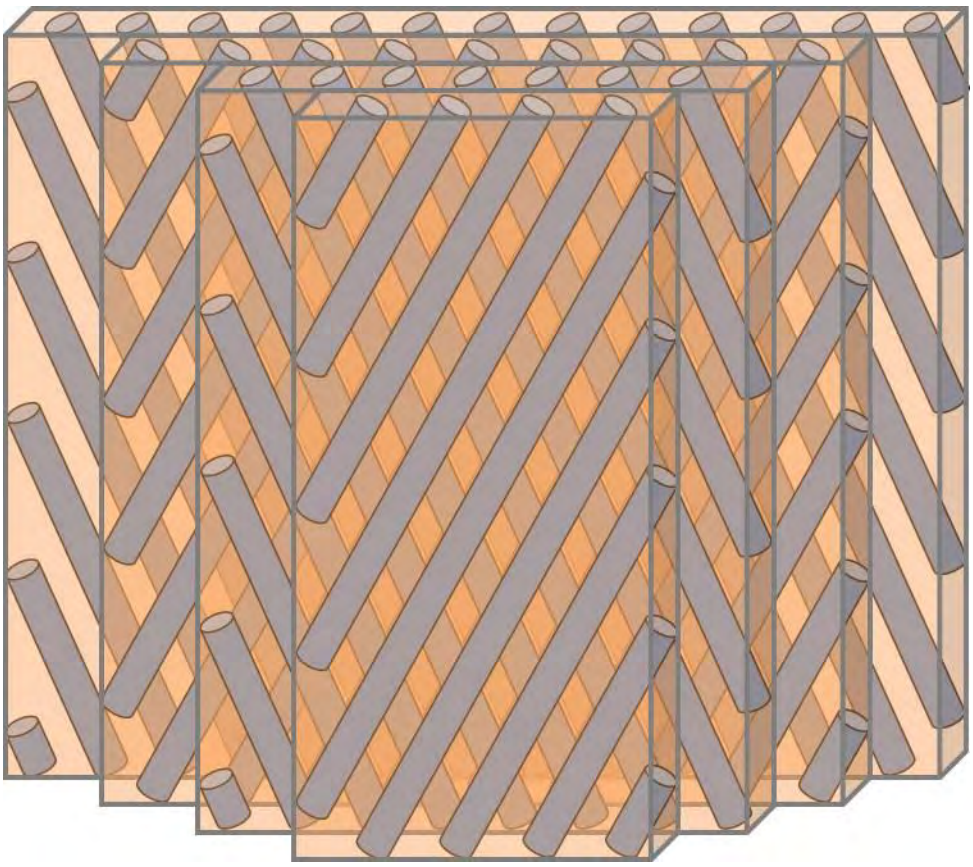

Figure 18. Osteon cross sectional view.

The SSV and SR-PNT views of cortical bone fiber orientation do not specify which osteonal layer contains what fiber direction [12], [64]. The studies are a focused view of a single section of bone. Additionally, due to the close-packed nature of adjacent Haversian systems, the overall material properties will be found through fractional volume percent of each fiber orientation.

The material properties of a single lamellar layer can be found by rotating the layer with respect to the 3-axis, as represented in Figure 15. This rotation can be completed by rotating the stiffness matrix of the material. The stiffness matrix is a combined view of the generalized Hooke's law. The two derivations of Hooke's law are shown in Equations 20-21 [72].

$$\begin{bmatrix} \sigma_1 \\ \sigma_2 \\ \sigma_3 \\ \sigma_4 \\ \sigma_5 \\ \sigma_6 \end{bmatrix} = \begin{bmatrix} c_{11} & c_{12} & c_{13} & c_{14} & c_{15} & c_{16} \\ c_{21} & c_{22} & c_{23} & c_{24} & c_{25} & c_{26} \\ c_{31} & c_{32} & c_{33} & c_{34} & c_{35} & c_{36} \\ c_{41} & c_{42} & c_{43} & c_{44} & c_{45} & c_{46} \\ c_{51} & c_{52} & c_{53} & c_{54} & c_{55} & c_{56} \\ c_{61} & c_{62} & c_{63} & c_{64} & c_{65} & c_{66} \end{bmatrix} \begin{bmatrix} \varepsilon_1 \\ \varepsilon_2 \\ \varepsilon_3 \\ \varepsilon_4 \\ \varepsilon_5 \\ \varepsilon_6 \end{bmatrix} \tag{20}$$

$$\begin{bmatrix} \varepsilon_1 \\ \varepsilon_2 \\ \varepsilon_3 \\ \varepsilon_4 \\ \varepsilon_5 \\ \varepsilon_6 \end{bmatrix} = \begin{bmatrix} s_{11} & s_{12} & s_{13} & s_{14} & s_{15} & s_{16} \\ s_{21} & s_{22} & s_{23} & s_{24} & s_{25} & s_{26} \\ s_{31} & s_{32} & s_{33} & s_{34} & s_{35} & s_{36} \\ s_{41} & s_{42} & s_{43} & s_{44} & s_{45} & s_{46} \\ s_{51} & s_{52} & s_{53} & s_{54} & s_{55} & s_{56} \\ s_{61} & s_{62} & s_{63} & s_{64} & s_{65} & s_{66} \end{bmatrix} \begin{bmatrix} \sigma_1 \\ \sigma_2 \\ \sigma_3 \\ \sigma_4 \\ \sigma_5 \\ \sigma_6 \end{bmatrix} \tag{21}$$

The *c* and *s* matrices are the stiffness and compliance matrices of the material, respectively. Due to the symmetric nature of the lamellar layers, the stiffness and compliance matrices are reduced to 6 independent constants. The stiffness matrix is shown below.

$$C_{ij} = \begin{bmatrix} c_{11} & c_{12} & c_{12} & 0 & 0 & 0 \\ c_{12} & c_{22} & c_{23} & 0 & 0 & 0 \\ c_{12} & c_{23} & c_{22} & 0 & 0 & 0 \\ 0 & 0 & 0 & c_{44} & 0 & 0 \\ 0 & 0 & 0 & 0 & c_{66} & 0 \\ 0 & 0 & 0 & 0 & 0 & c_{66} \end{bmatrix} \tag{22}$$

The C_{ij} and S_{ij} matrices are the inverse of each other. In order to enact a rotation of each lamellar layer, the stiffness matrix will be rotated. The stiffness matrix can be found by inverting the compliance matrix of each lamellar layer. The normal and shear properties were derived independently for each material, allowing the compliance matrix to be built.

$$S_{ij} = \begin{bmatrix} 1/E_1 & -\nu_{21}/E_1 & -\nu_{21}/E_1 & 0 & 0 & 0 \\ -\nu_{21}/E_1 & 1/E_{23} & -\nu_{32}/E_{23} & 0 & 0 & 0 \\ -\nu_{21}/E_1 & -\nu_{32}/E_{23} & 1/E_{23} & 0 & 0 & 0 \\ 0 & 0 & 0 & 1/G_{23} & 0 & 0 \\ 0 & 0 & 0 & 0 & 1/G_{12} & 0 \\ 0 & 0 & 0 & 0 & 0 & 1/G_{12} \end{bmatrix} \tag{23}$$

In order to solve for the stiffness matrix, Equation 23 is inverted. This matrix can then be rotated according to a newly defined set of axis. Equation 24 defines the rotated material properties.

$$\sigma' = C'\varepsilon' \tag{24}$$

The prime notation indicates the newly rotated axis coordinates, where C' is the stiffness matrix of the original material. In order to solve for the C matrix along the original axes, the stress and strain must be transformed.

$$T_\sigma \sigma = C' T_\varepsilon \varepsilon \tag{25}$$

By inverting T_σ and pre-multiplying into the right side of Equation 25, the generalized Hooke's equation is found.

$$\sigma = T_\sigma^{-1} C' T_\varepsilon \varepsilon \tag{26}$$

Equation 26 shows that the stiffness matrix along the new coordinates can be defined as:

$$C = T_\sigma^{-1} C' T_\varepsilon \tag{27}$$

where T_σ^{-1} is the inverse of the stress transformation matrix and T_ε is the transformation matrix of the engineering strain. The transformation matrices are defined in Equations 28-29.

$$T_\sigma^{-1} = \begin{bmatrix} m^2 & n^2 & 0 & 0 & 0 & -2mn \\ n^2 & m^2 & 0 & 0 & 0 & 2mn \\ 0 & 0 & 1 & 0 & 0 & 0 \\ 0 & 0 & 0 & m & n & 0 \\ 0 & 0 & 0 & -n & m & 0 \\ mn & -mn & 0 & 0 & 0 & \left(m^2 - n^2\right) \end{bmatrix} \tag{28}$$

$$T_\varepsilon = \begin{bmatrix} m^2 & n^2 & 0 & 0 & 0 & mn \\ n^2 & m^2 & 0 & 0 & 0 & -mn \\ 0 & 0 & 1 & 0 & 0 & 0 \\ 0 & 0 & 0 & m & -n & 0 \\ 0 & 0 & 0 & n & m & 0 \\ -2mn & 2mn & 0 & 0 & 0 & \left(m^2 - n^2\right) \end{bmatrix} \tag{29}$$

$m = \cos\theta$ and $n = \sin\theta$, where θ is defined as rotation about the 3 axis.

In addition to accounting for the rotation of the individual lamellar layers, the Haversian canal and canaliculi will be addressed in the macroscale model. Based on the dimensions of the Haversian system, the Haversian canal and the microscopic canaliculi, macroscale cortical bone is 75% densely packed bone and 25% void space. As with smaller scale models the void space will be addressed as a liquid in compression and a void in tension.

b. Fiber Direction

In order to calculate the composite properties of cortical bone, two models will be assessed. One model utilizes the preferential orientations found by [12] while the other model assumes a continuous twist as found by [64]. These two models will be referred to as preferential orientation and smooth orientation, respectively, from this point on.

The two models rely on volume percent of a defined fiber orientation. The volume percentages present for each fiber orientation of the preferential model are shown in Table 20 and the designated volume percentages for the smooth model are shown in Table 21.

Table 20. Preferential orientation layered composite model parameters.

Fiber Designation	Fiber Direction	Volume Percent
Transverse	72.5°	45
Longitudinal	22.5°	35
Intermediate	0°	5
Intermediate	40°	5
Intermediate	55°	5
Intermediate	90°	5

The transverse and longitudinal fibers are set at the average of the range defined by [12]. The intermediate fibers are split between four intermediate directions, at 5% volume each.

Table 21. Smooth orientation layered composite model parameters.

Fiber Direction	Volume Percent
0°	10
10°	10
20°	10
30°	10
40°	10
50°	10
60°	10
70°	10
80°	10
90°	10

The fiber distribution for the smooth orientation model represents a consistent fanning angle. The stiffness matrix of each layer is calculated using Equation 28, using the fiber directions listed in Table 20 and Table 21 as the theta values for Equations 29-30. The Voigt estimation of composite stiffness is calculated for the volume percent shown in Table 20 and Table 21. It should be noted that the rotation of fiber directions is assumed symmetrical about 0°. The fiber directions as stated by [12] and [64] do not designate either positive or negative angles about the longitudinal axis. Therefore, the results of the layered composite for cortical bone model are expected to produce an orthotropic linear elastic material. However, due to the random radial distribution of osteons, we should expect a transverse isotropic material. Therefore, the average of the S_{12} and S_{13} will be used to calculate ν_{21}, the average of S_{22} and S_{33} will be used to find E_{23} and ν_{32}, and the average of S_{55} and S_{66} will be used to find G_{12}.

c. Cortical Model Results

The results of the layered composite model were calculated using only the linear fibril model. Additionally, the preferential and smooth layered models were calculated in both tension and compression. The compressive results are shown in Table 22 while the tensile results are shown in Table 23.

Table 22. Cortical bone in compression

	50% EFM		70% EFM		90% EFM		95% EFM	
	Pref.	Smooth	Pref.	Smooth	Pref.	Smooth	Pref.	Smooth
E_1 [GPa]	5.074	4.642	5.390	4.914	5.944	5.453	6.424	5.923
E_{23} [GPa]	5.836	5.679	6.217	6.045	6.818	6.586	7.282	6.990
G_{23} [GPa]	0.700	0.735	0.773	0.818	0.839	0.889	0.870	0.920
G_{12} [GPa]	0.944	0.957	1.037	1.050	1.144	1.157	1.213	1.226
ν_{21}	0.319	0.357	0.316	0.355	0.311	0.350	0.306	0.344
ν_{32}	0.232	0.226	0.227	0.221	0.222	0.219	0.218	0.218

The preferential fiber orientation exhibits greater stiffness for all % EFM values tested. Additionally, the stiffnesses and shear moduli increase for increasing % EFM, as is expected. The shear moduli in the 23 direction and Poisson's ratio in the 23 direction are similarly matched between models.

Table 23. Cortical bone in tension.

	50% EFM		70% EFM		90% EFM		95% EFM	
	Pref.	Smooth	Pref.	Smooth	Pref.	Smooth	Pref.	Smooth
E_1 [GPa]	4.110	3.704	4.396	3.930	4.622	4.120	4.696	4.193
E_{23} [GPa]	4.779	4.649	5.138	5.009	5.408	5.286	5.485	5.371
G_{23} [GPa]	0.666	0.699	0.735	0.778	0.798	0.846	0.829	0.876
G_{12} [GPa]	0.887	0.900	0.970	0.983	1.039	1.054	1.069	1.085
ν_{21}	0.375	0.427	0.378	0.432	0.398	0.455	0.423	0.482
ν_{32}	0.257	0.250	0.256	0.247	0.268	0.257	0.284	0.272

The results for tension are similar to those in compression. The preferential model exhibits greater stiffnesses for all models. Additionally, the shear moduli and Poisson's ratio in the 23 direction are also similarly matched for models. For both compressive and tensile tests, the preferential and smooth models produce similar results. For this reason, we can assume that the physical orientation of the fibers does not drastically affect the stiffness of cortical bone.

3. Cortical Model Discussion

The results of the cortical model can be compared to results from experimental and theoretical testing. These results are shown in Table 24.

Table 24. Comparison of values for cortical results.

Elastic Modulus [GPa]	Method	Source
6	FEM, 20% Mineral Volume Fraction	[1]

Elastic Modulus [GPa]	Method	Source
9	FEM, 30% Mineral Volume Fraction	[1]
15	FEM, 40% Mineral Volume Fraction	[1]
21	FEM, 50% Mineral Volume Fraction	[1]
7.28	Microdisplacements by Machine Vision Photogrammetry	[73]
17.5±1.9	Uniaxial Tension	[74]
17.8±2.1	Uniaxial Tension	[75]
12-22	Assumptions	[8]
19.1±5.4	Nanoindentation (Transverse)	[76]
17.1±3.15	Uniaxial Compression and Tension[1]	[77]
17.0	Uniaxial Compression and Tension	[78]
14.91±0.52	Acoustic Microscopy (Transverse)	[79]
20.55±0.21	Acoustic Microscopy (Longitudinal)	[79]
16.58±0.32	Nanoindentation (Transverse)	[79]
23.45±0.21	Nanoindentation (Longitudinal)	[79]
22.5±1.3	Nanoindentation (Longitudinal)	[80]

[1]Only two femurs sampled had statistically significant differences in compression and tension

The experimental stiffnesses shown in Table 24 determine that our model underestimates the longitudinal stiffness of cortical bone. This could be due to several factors, but it is most likely due to the assumptions made at various hierarchies. Furthermore, the similarity of tensile and compressive testing of human cortical samples could be due to the posthumous treatment of samples. Bone is kept wet throughout machining and processing, however, saline solution is not always used. The use of regular water can affect the ion balance and presence of water at the nanoscale. Additionally, the bone is not always kept at physiological temperatures. The most profound effects may be due to freezing of the samples. The expansion of the liquid in the void spaces may have altered the results. Additionally, water exists as a very tightly bound column in TC molecules. The freezing of these molecules may disrupt their structure, affecting results in tension and compression.

The finite element model listed for comparison in Table 24 found lower estimates of stiffnesses for two of the four mineral volume fractions tested. Only at higher mineral volumes does the FEM approach the values found through experimental testing. The

stiffnesses found from this study are proportional to mineral fraction volume. Table 19 lists the mineral volume fractions for the different %EFM tested. This study utilizes a maximum of 25% mineral volume fraction which yielded a longitudinal stiffness of approximately 7 GPa. From the FEM listed above, the results would predict a longitudinal stiffness of approximately 7.5 GPa. This shows that the relatively simple models presented match those of complex finite element models. It can also be reasoned that increasing the mineral volume fraction in this study will alter the macroscale results.

While most accepted results of human bone material properties depict longitudinal or transverse stiffness, several studies have been completed that analyze the orthotropic properties of bone. These values are shown in Table 25.

Table 25. Elastic moduli of compact bone. All stiffnesses are in GPa.

Location	Femur	Tibia	Femur	Femur	
Method	Ultrasound	Mechanical Testing	Ultrasound	Ultrasound	Preferential Model 95%EFM, Compression
Source	[78]	[81]	[82]	[83]	This Study
E_{11}	11.17	6.94	13.18	18.57	6.42
E_{22}	11.17	8.56	14.56	19.43	6.39
E_{33}	17.21	18.45	21.67	28.29	8.46
G_{23}	3.3	4.91	6.56	8.71	0.87
G_{13}	3.3	3.56	5.85	8.71	0.97
G_{12}	3.6	2.41	4.74	8.71	1.62
ν_{12}	0.595	0.495	0.377	0.323	0.419
ν_{13}	0.298	0.142	0.237	0.209	0.191
ν_{23}	0.298	0.119	0.225	0.126	0.193

The values depicted above are the orthotropic material properties. The raw values of the preferential fiber model, with 90% EFM and in compression, are shown in Table 25. These values do not compensate for transverse isotropic assumptions. The model presented in this study exhibits similar trends as the experimental tests. The stiffness in the 3 direction is greater than both the stiffnesses in the 1 and 2 directions. The

orthotropic bone properties confirm that this study produces an underestimate of material properties. Moreover, the results shown in Table 25 oppose the assumption that small sections of macroscale bone are transversely isotropic.

One of the four measurements of the elastic moduli assumes transverse isotropy. The other three measured orthotropic material properties. These properties are defined for small samples, not single osteons. Additionally, the differences between transverse isotropic and orthotropic measurements are small. Large deviations have been credited to regions of greater porosity [84]. As a whole, cortical bone exhibits orthotropic symmetry, or a higher degree of symmetry [85]. This means that the minimum level of symmetry is orthotropic symmetry, but regions of transverse isotropy or isotropy may exist. These higher symmetries can be attributed to the packing of Haversian systems [85]. Hexagonal and random packing can be identified as transversely isotropic. Due to the preferential alignment of the Haversian canal to the long axis of the bone, the assumption that cortical bone is transverse isotropic can be validated for ideal materials. The imperfections of living tissues may cause lower order symmetry.

In addition to the anisotropic properties of bone, the void spaces present in bone may not be randomly distributed. The ability of bone to sense the stress field is hypothesized to be from the cell processes located within the void space of lamellar layers [12]. It can be extrapolated that the canaliculi are aptly located so as to optimally sense the mechanical state of the surrounding bone. Thus, it can be derived that the void space of bone is a non-random occurrence.

The alternating orientation of lamellar layers had little impact on the stiffness of cortical bone. However, this twisting is thought to aid in resisting crack propagation [64]. This can help increase fracture toughness and prevent damage from propagating from one lamellar layer to the next.

C. CANCELLOUS BONE

Cancellous bone is a porous macrostructure that consists of small plates and rods. The porous nature of cancellous bone allows for it to house bone marrow and to reduce

the weight of the skeletal system [6]. The individual rods of cancellous bone are known as trabeculae.

1. Three Dimensional Cancellous Structure

Cancellous bone is more metabolically active than cortical bone. This activity leads to more frequent absorption and deposition of bone. Additionally, the deposition of new bone is related to the applied stresses on the cancellous bone [9], [86], [87]. As a result of the directed deposition of lamellar layers, the outermost layers of trabecular bone are oriented parallel to the longitudinal axes of the trabeculae [9]. The adjacent layers vary slightly in their orientation, as they were formed under a different state of stress. The resulting structure of a trabecula is that of lamellar layers that follow a relatively uniform fiber direction. This is shown in Figure 19.

Figure 19. Trabecular bone lamellar layer orientation, from [9].

The layers intersect at low angles, with respect to the longitudinal axis of the trabecula. As a result, the properties of a single trabecula can be found through a

laminated composite constructed of a -10°/-5°/0°/5°/10° layered motif. The center of the strut, indicated by the star in Figure 19, shows a remnant of the original trabecular network [9], which has yet to be regrown. These remnants will be assumed to exhibit similar material properties to the lamellar layers. This will cause the model to have a slightly overestimation of the longitudinal modulus, since more lamellar layers are assigned to the longitudinal axis.

While a laminated composite material represents the material properties of a single trabecula, it does not quantify the properties of cancellous bone. The structure of cancellous bone is a uniquely three dimensional problem, that cannot be solved through a two dimensional approximation [88]. Additionally, there is much heterogeneity in cancellous bone at different anatomical locations [89].

Early models of cancellous bone utilized a model of rods and plates. Four early models were an asymmetric rod-like cubic model, a plate-like cubic model, a rod-like hexagonal columnar model, and a plate-like hexagonal columnar model [87]. These early models helped to shape simple models of cancellous bone. However, these models provided asymmetrical properties for cancellous bone. Additionally, the early models included Euler buckling as a failure mechanism [87]. Later experiments have shown that failure of cancellous bone is most commonly due to microscopic cracking, which removes buckling as a failure mode for trabeculae [90].

With the decrease in cost and increase in speed of computing, complex finite element models have been used to model cancellous bone. Three dimensional models formed from micro-computed tomography can replicate small sections of bone [91]. Furthermore, two unit cells have been proposed that are able to accurately model cancellous bone. Kadir et al. [91] compared the results of prismatic unit cells and tetrakaidecahedral unit cells to those of a micro-computed tomography model. The authors found that both unit cells accurately represent the mechanical properties. Additionally, Guo and Kim [92] have shown that a complex finite element model of several tetrakaidecahedron cells can accurately represent different levels of bone loss due to ageing.

This study will make use of a tetrakaidecahedron unit cell to calculate the macroscale properties of cancellous bone. Several values of trabecular bone properties will be used, as well as different bone densities. The results of the macroscale properties will then be compared to experimental data.

2. Trabecular Bone Model

Trabecular bone will be modeled by the same layered composite model as utilized for cortical bone. However, the fiber orientations and volume percent of each layer will be altered.

a. Trabecular Model Parameters

The parameters for trabecular bone are listed in Table 26.

Table 26. Trabecular bone layered composite model parameters.

Fiber Direction	Volume Percent
-10°	20
-5°	20
0°	20
5°	20
10°	20

Due to the lack of Haversian canals in trabecular bone, the void space is direct a result of microscopic canaliculi. This void space will be evaluated at 5% volume percent and will be treated as a liquid in compression and a void in tension.

b. Trabecular Results

The results of the trabecular laminated composite model for both compression and tension are shown in Table 27.

Table 27. Trabecular bone in compression and tension.

	50% EFM		70% EFM		90% EFM		95% EFM	
	Comp.	Tens.	Comp.	Tens.	Comp.	Tens.	Comp.	Tens.
E_1 [GPa]	6.047	5.099	6.427	5.158	7.848	5.223	9.451	5.245
E_{23} [GPa]	8.519	7.762	9.186	8.569	9.782	9.134	9.975	9.252
G_{23} [GPa]	1.259	1.197	1.461	1.389	1.605	1.526	1.636	1.555
G_{12} [GPa]	0.658	0.623	0.672	0.636	0.717	0.673	0.773	0.720
ν_{21}	0.242	0.254	0.235	0.264	0.236	0.318	0.241	0.382
ν_{32}	0.234	0.253	0.232	0.241	0.240	0.237	0.248	0.237

The results in compression are stronger than the results in tension for all models. The difference between tensile and compressive stiffnesses magnifies for increasing %EFM. The results of the trabecular bone model can be compared to experimental and theoretical results. Early models tested macroscale cancellous bone in order to back calculate the material properties of trabecular bone. Current methods directly measure trabecular material properties through the use of microelectromechanical systems and nanoindentation. Table 28 lists the experimental and theoretical results for trabecular bone.

Table 28. Comparison of values for trabecular results.

Elastic Modulus [GPa]	Method	Source
18.5±1.5	Assumption	[93]
11.38	Inelastic Buckling	[94]
12.7±2.0	Ultrasound (Isotropic)	[95]
15	Microhardness (Transverse)	[96]
3.81	Three-point bending	[97]
5.35±1.36	Four-point bending	[98]
10.4±3.5	Tensile Test	[99]

14.8±1.4	Ultrasound (Isotropic)	[99]
13.4±2.0	Nanoindentation (Transverse)	[80]
18.0±2.8	Tension and Compression Tests	[75]
11.4±5.6	Nanoindentation (Transverse)	[76]
17.5±1.12	Acoustic Microscopy (Transverse)	[79]
18.14±1.7	Nanoindentation (Transverse)	[79]

The results for trabecular bone are similar to those of cortical bone, as the model used in this study underestimates the stiffness values. However, the trabecular model is closer to the mean values of accepted longitudinal and transverse results. The values established from bending tests were found by testing machined samples of bone. The same post-processing issues that affected the measurement of cortical bone will affect the measurements of trabecular bone.

3. Tetrakaidecahedron Finite Element Model

The computation of a unit-cell model for cellular materials was developed by Kwon, et. al. [100]. This model utilizes a tetrakaidecahedron (4KDH) unit cell as the base unit. The 4KDH is a regular truncated octahedron and was developed by Lord Kelvin in 1887 as an attempt to model soap bubble formation in foam. A 4KDH provides minimum surface area for a given volume [100]. Additionally, the 4KDH cell is space filling, meaning that its faces uniformly intersect with adjoining cells [101]. Visualization of the 4KDH structure is shown in Figure 20.

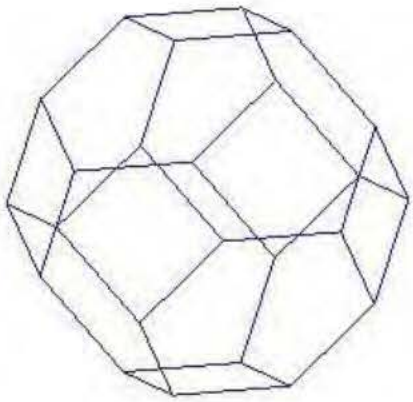

Figure 20. Tetrakaidecahedron, from [101].

The 4KDH has eight hexagonal faces, six square faces, 36 edges and 24 vertices. For the open cell structures present in cancellous bone, the faces are treated as voids and the edges are treated as trabeculae. A simple finite element model was developed by [100] to analyze the 4KDH frame.

The 4KDH unit cell is a cube, where the frame structure is composed of uniform circular beams. The cross-section of the frame elements are dependent on the volume fraction defined for the unit-cell [100]. Each frame element is defined by one node at each end. The model utilizes six degrees of freedom: displacement and rotation about each of the three axes. Loads applied to the model are applied at the vertices. It is assumed that the beams do not buckle. Furthermore, the finite element model developed by [101] was developed through Galerkin's methods and linear shape functions, and assumes linear elastic behavior.

The finite element model is based on forces applied to the model and the stiffness of the edge elements. This relationship is defined in Equation 30.

$$[K]\{d\} = \{F\} \tag{30}$$

where $[K]$ is the global stiffness matrix, $\{d\}$ is the nodal displacement and $\{F\}$ is the applied forces. The elemental stiffness matrix is defined in Equation 31 [101].

$$\left[K^e\right] = \begin{bmatrix} K_{11}^e & K_{12}^e \\ K_{21}^e & K_{22}^e \end{bmatrix} \tag{31}$$

Furthermore, the stiffness of each frame element must be rotated based on its direction cosines in order to include it in the global stiffness matrix. The complete matrix representation of the 4KDH model is shown in the Appendix.

The FEM model for the 4KDH produces isotropic material properties. Therefore, from an applied load, the material's Young's modulus can be calculated from the resultant strains. Additionally, since each frame element is treated as an isotropic material, two variations will be assessed: one using the compressive material properties and one using the tensile material properties. This will create a bound on the material properties of cancellous bone for each percent extrafibrillar mineralization used.

4. Cancellous Bone Model Parameters

In order to assess the material properties of cancellous bone, several parameters must be identified. The 4KDH model calls for isotropic material properties. Since the frame elements of the model are long beams, the material properties of the trabecular long axis will be the dominant material properties. Therefore, the longitudinal stiffness and shear modulus will be used. These properties for the different %EFM, in tension and in compression, are listed in Table 27. Furthermore, the effects of bone marrow will be ignored in this study. Bone marrow has little ability to resist shear [102], diminishing its ability to act as an elastic foundation for the beam elements.

The radius of the beam elements and the volume density of the bone must be defined. A universally accepted set of indices have been identified that help to address cancellous structure: bone volume per tissue volume (BV/TV), bone surface per tissue volume (BS/TV), bone surface per bone volume (BS/BV) [89]. These indices can help to derive the structure of the trabeculae: trabecular thickness (Tb.Th), trabecular separation (Tb.Sp), and trabecular number (Tb.N) [89].

a. Model Overview

Cancellous indices for various anatomical locations have been defined. Table 29 lists the two indices most pertinent to the 4KDH model and identifies the anatomical location of the measurements.

Table 29. Anatomical cancellous bone indices.

BV/TV	Tb.Th (mm)	Anatomical Location	Source
0.2654		Femoral Neck	[103]
0.2067	0.172	Femoral Head	[104]
0.27	0.2	Distal Femur	[105]
0.27	0.19	Proximal Femur	[105]
0.105		Greater Trochanter	[103]
0.111		Tibia	[103]
0.34	0.36	Radius	[106]
0.41	0.33	Distal Tibia	[107]
0.27	0.47	Distal Tibia	[107]
	0.186	Average (Young Age)[1]	[108]
	0.174	Average (Medium Age)[1]	[108]

[1]Young age is defined as 16-39 years-old and medium age is defined as 40-59 years-old

The measurements taken by [107] were used for comparison of high-resolution peripheral quantitative X-ray microtomography to the standardized measurements taken by magnetic resonance imaging. Therefore, the differences in BV/TV and Tb.Th of the distal tibia are due to the different measurement techniques. This study will make use of the measurements of the femur, as it is the most tested bone in the human anatomy.

b. Tetrakaidecahedron Model Parameters

In order to utilize the 4KDH model, the diameters of the beam elements are set to the average thickness of the femoral trabeculae. This was calculated as 0.19 mm, from the indices defined in the femoral measurements. Additionally, the BV/TV index was used to define the beam element length. The length was calculated so that the relative volume of the 4KDH unit cell matches that of the trabecular unit cell. The load applied to each model was derived from the area of the 4KDH unit cell face so that a constant stress was analyzed. This study will calculate the effective stiffnesses of the three femoral indices: the femoral neck, the femoral head and the distal/proximal femur. All calculations assume a constant trabecular diameter of 0.19 mm.

c. Model Results

The results of the 4KDH model were calculated using the trabecular results in compression and tension. These two values will be used to create bounds on the stiffness of cancellous bone. The results of the three anatomical locations are shown in Table 30.

Table 30. Cancellous model results, all stiffnesses expressed in MPa.

	50% EFM		70% EFM		90% EFM		95% EFM	
	Comp.	Tens.	Comp.	Tens.	Comp.	Tens.	Comp.	Tens.
Femoral Neck	292	246	311	249	379	252	457	253
Femoral Head	196	165	209	167	255	170	307	170
Distal/Proximal	300	253	319	256	390	259	469	260

The results of the cancellous model are stiffer in compression than tension for all models. Additionally, the distal and proximal femur is stiffer than both the femoral neck and head. This is expected, due to its greater density. The results of the cancellous model can be compared to experimental and theoretical results.

5. Cancellous Model Discussion

The accepted values of cancellous bone are shown in Table 31.

Table 31. Comparison of values for cancellous results.

Elastic Modulus [MPa]	Method	Source
47±2	Finite Element Method	[109]
300±200	Micro-compression testing	[110]
110±90	Compressive Testing	[111]
385±315	Estimation	[8]
550±450	Mechanical Testing	[112]

The accepted values are in agreement with the values found in this study. However, due to the underestimation of previous hierarchies, a similar underestimate should be expected for cancellous bone. The results of the cancellous model produce elastic moduli greater than expected. This could be due to several causes. The assumed isotropy of cancellous bone is a broad assumption. Orthotropic elastic moduli have been measured through ultrasonic measurements [113]. However, the calculation of orthotropic materials for this study would require a complex model based on a specific anatomical site. Utilizing a generalized 4KDH unit cell, an isotropic stiffness was calculated that confirms the validity of previous hierarchies. This is a computationally inexpensive model that is not site specific.

The results of the cancellous model help identify the reduced stiffness of the porous structure. The physiological purpose of cancellous bone is to provide lightweight structural support to abnormal volumes of skeletal bone. Additionally, the porous structure of cancellous bone provides a cellular infrastructure for bone marrow, creating a large surface area for metabolic activity. Furthermore, the in vivo trabecular network has

been optimized through repeated applied stresses. The trabeculae respond to the applied mechanical loads [9], [86], [87]. Due to this, the in vivo mechanical properties of cancellous bone should be greater than those found through experimental results.

THIS PAGE INTENTIONALLY LEFT BLANK

V. ANALYSIS

In order to analyze the robust nature of the models presented in this study, changes to the different hierarchies will be assessed. Additionally, the key hierarchy will be identified that has the greatest influence on the macroscale values. In order to assess the overall effects of the model, we must establish a control model. From the results of the fiber model, we can expect a high level of extrafibrillar mineralization within living bone. Additionally, the linear fibril model was assumed to be the proper fibril crystal packing method due to the assessed mineral volume. Therefore, the control model will be comprised of the linear fibril HA packing and 95% EFM. Moreover, the model will only be tested in compression. The macroscale cortical model will assume a preferential fiber orientation, since the results of the two cortical models are similar.

The results that will be assessed for macroscale models will be longitudinal stiffness, transverse stiffness, and mineral volume fraction. Additionally, the results of the modified hierarchy will be assessed in comparison to cortical and trabecular values, as the results of cancellous bone are not as robust as those of trabecular bone. A separate analysis will be completed to assess bone loss. In order to analyze the effects of bone loss on the properties of cancellous bone, different bone densities will be evaluated using the FEM presented for macroscale cancellous bone.

A. MODIFIED HIERARCHY

This analysis will make changes at all microscale and macroscale hierarchies in order to assess their contribution to cortical and trabecular properties. At the microscale level, the fibrillar subunit will be altered. Additionally, the diameter of the fibrils and the thickness of the EFM will be adjusted. At the macroscale, the dimensions of the fiber and the disordered matrix will be adjusted. Lastly, both the Voigt and Reuss averages of cortical and trabecular bone will be found. These two models create an upper and lower bound on the stiffness of a composite based on volume fraction of each constituent [114].

1. Hierarchical Adjustments

The adjustments to the hierarchy will be completed individually. The adjustments will first be described and the results of all adjustments will be compared to the control model. The first alteration will be made to the unit cell of the fibrillar model. The dimensions of the HA crystal will remain the same, but the volume of the surrounding TC matrix will be reduced. The dimensions shown in Table 32 will be used.

Table 32. Unit cell alteration to fibrillar model.

Dimension	*Model 1* Value [nm]	*Model 2* Value [nm]	*Model 3* Value [nm]
a_1	50	50	50
a_2	17	17	17
b_1	25	25	25
b_2	3	1	1
c_1	3	3	3
c_2	6	6	3

These alterations will increase the mineral volume percent of the fibrillar model while also changing the material properties. The next hierarchy to be altered is that of the bone fiber. The model of the fiber relies on volume percent of both the bone fibril and the extrafibrillar mineral. Two variations will be tested that alter the volume percent of the fibril. The original model assumed a 72.25 vol% fibril. The first alteration will assume a 62.25 vol% fibril and the second alteration will assume an 82.25 vol% fibril. These variations will be referred to as Model 4 and Model 5, respectively.

The only component of the macroscale hierarchies that will be adjusted is that of lamellar bone. The properties of lamellar bone were calculated by discerning the volume percent of bone fibers in the disordered fibrillar matrix. The original model was composed of only 38.44 vol% fiber. The adjusted models will increase the fiber volume percent in order to compare results. Model 6 will assume 50 vol% fiber, Model 7 will assume 70 vol% fiber, and Model 8 will assume 90 vol% fiber.

2. Adjustment Results

The results of Models 1 through 8 are shown in Table 33. These models adjust only the hierarchy discussed, leaving all other levels with their original geometry.

Table 33. Results of adjusted hierarchies, stiffnesses shown in GPa.

Model	*Cortical Bone*				*Trabecular Bone*				Mineral Volume Fraction [%]
	Voigt		Reuss		Voigt		Reuss		
	E_1	E_{23}	E_1	E_{23}	E_1	E_{23}	E_1	E_{23}	
1	7.05	8.03	3.75	4.48	10.28	11.19	8.04	9.00	29.97
2	8.27	9.53	3.92	4.72	11.63	13.87	8.76	10.48	31.50
3	10.26	11.87	4.33	5.15	14.18	17.73	10.20	12.49	42.18
4	6.95	7.87	3.58	4.33	10.79	10.64	8.15	8.60	28.03
5	5.84	6.61	3.61	4.23	8.15	9.07	6.84	7.72	22.00
6	7.21	8.30	3.35	4.21	10.49	11.84	7.77	9.12	27.53
7	8.93	10.49	2.75	3.81	12.29	16.07	7.68	10.34	31.89
8	11.25	13.39	1.81	2.84	14.08	22.04	6.38	10.05	36.22
Original	6.42	7.28	3.58	4.29	9.45	9.98	7.52	8.24	25.01

The results show that the transverse stiffness is greater than longitudinal stiffness for all models. A general trend can be seen that increasing mineral volume fraction increases macroscale stiffnesses. Additionally, reducing the TC matrix within the fibrillar subunit increases macroscale properties. Increasing the volume percent of the fibril within the fiber model has an inverse effect on its stiffness. This is due to the extra fibrillar mineral. The less volume that is occupied by the fibril, the more volume is occupied by the mineral. Increasing the size of the bone fibers within the lamellar layers increases the macroscale stiffnesses.

Furthermore, several trends can be identified between the Voigt and Reuss models. The Voigt model assumes isostrain conditions, whereas the Reuss model assumes isostress conditions [114]. Thus, the Voigt is the upper bound of the material properties while the Reuss is the lower bound. These are derived by averaging the stiffness matrices or the compliance matrices, respectively. The results of the cortical model show a large difference between the Voigt and Reuss models. This is due to the

large theta values of the rotated layers. The trabecular models show less variation because the layers are constrained to small thetas.

Furthermore, the most influential hierarchy is the fibrillar model. Small changes in the basic hierarchy are compounded throughout the upper levels. Changes to the fibrillar model can be physically embodied by reducing the vertical spacing between HA crystals. The second most influential hierarchy is that of the lamellar layers. The relatively small volume percent of fibers present in the original model allowed for large increases in fiber diameter. This increase in fiber diameter decreases the relative proportion of fibrillar matrix.

3. Optimized Adjustment

The parameters of several hierarchies were adjusted simultaneously in an attempt to optimize the macroscale results. At the microscale, both the fibrillar subunit and fiber models were adjusted. The fibrillar subunit utilized the unit cell dimensions of Model 2. The fiber model assumed a fibril vol% of 60%. The lamellar model assumed a fiber vol% of 70%. The results from the model are shown in Table 34.

Table 34. Optimized macroscale bone properties.

	Cortical		Trabecular	
	Voigt	Reuss	Voigt	Reuss
E_1 [GPa]	12.71	2.82	16.72	8.91
E_{23} [GPa]	15.03	3.98	24.17	12.73
G_{23} [GPa]	0.914	0.004	2.18	0.020
G_{12} [GPa]	1.62	0.004	0.52	0.019
ν_{21}	0.272	0.413	0.165	0.304
ν_{32}	0.153	0.176	0.164	0.176

The optimized hierarchy of bone contained 43.82% mineral volume fraction. The values of E_1 for both models and the value of E_{23} for the cortical model are within the range of accepted values. Transverse stiffness of the trabecular model is greater than

expected. Additionally, the results can be compared to the orthotropic material properties of cortical bone shown in Table 25. The cortical shear moduli and ν_{21} values are slightly lower than the tested values, although the Young's moduli are within normal bounds.

The accepted stiffnesses of cortical bone are greater than those of trabecular bone. The results from this study show that the trabecular material is stiffer than the cortical material. Current theories accept that the only difference between trabecular and cortical material is the volume fraction of fiber orientations, which is respected in this study. Therefore, discrepancies in material stiffness are due to variations at the microscale hierarchies.

This could be due to several assumptions, such as the assumption that the lamellar layers at the center of trabecular struts exhibit the same material properties as the younger bone. The layers should physically portray lamellar layers that are similar in orientation to the surface layers. However, this assumption is unique for each individual strut based on its historical loading. It can be hypothesized that each trabecular strut exhibits different mechanical properties, independent of its dimensions. This makes the quantification of cancellous material properties very difficult, even with complex finite element models.

Additionally, the differences could be due to the simplification of void space within the macrostructures. The cortical bone models account for 25% void space due to the combination of Haversian canals and canaliculi. The trabecular model identifies only 5% void space due to the lack of Haversian canals. However, the void spaces were theorized to be in locations that improved the mechanosensation of the cells that directed bone growth. Therefore, the complex geometry of cortical and trabecular bone may require more than a volume fraction analysis to determine the implications of void space.

B. EFFECTS OF BONE LOSS

Bone loss is an identifiable side effect of both age and disease. Several studies have identified quantitative differences between healthy individuals and individuals suffering from bone loss. The differences are shown with respect to the cancellous indices of BV/TV and Tb.Th. The effects of bone loss are shown in Table 35.

Table 35. Cancellous bone indices for individuals with bone loss.

BV/TV	Tb.Th (mm)	Anatomical Location	Group Identifier	Source
0.26	0.33	Distal Radius	Osteoporotic Postmenopausal Females	[106]
	0.157	Proximal Tibia	60-79 years-old	[108]
0.16		Iliac Crest	70-90 years-old	[115]

While no results are shown for the human femur, the indices shown in Table 35 identify both a reduction in BV/TV and a thinning of trabeculae. In order to analyze the effects of reductions in bone density, both modes of bone loss will be tested. The cancellous model will assume baseline values of 0.27 and 0.19 mm for BV/TV and Tb.Th, respectively. The models will utilize the optimized material properties of trabecular bone, as found through Voigt averaging, and will test only in compression. The baseline cancellous results are re-calculated for the optimized trabecular properties.

Table 36. Cancellous bone material properties after bone loss.

BV/TV	Tb.Th [mm]	Stiffness [MPa]
0.27	0.19	830
0.24	0.19	689
0.20	0.19	514
0.16	0.19	357
0.27	0.17	830
0.27	0.15	830
0.27	0.13	830

The results of the cancellous model highlight a weakness of the finite element model. The FEM utilizes a ligament radius and length. In order to assign a BV/TV ratio, the radius is defined and the ligament length is calculated. Changes to the trabecular thickness do not affect cancellous stiffness as the length of the elements is also reduced to account for a steady BV/TV.

The results show a steady decrease in macroscale stiffness as a result of decreasing density. This shows that the effects of a 10% reduction in density results in a

50% reduction in stiffness. Furthermore, the effects of the trabecular thinning may apply more to the failure modes of trabecular bone than to the material properties.

C. HELICAL MODEL

Early models of osteons speculated that the angular orientation of bone fibers acted as spring stiffeners. They assumed that the twisting fibers within a lamellar layer act as springs [9]. The stiffness of an osteon can then be found by summing the stiffnesses of the individual springs. This is similar to the model used for the calculation of tropocollagen material properties. We can test the validity of this assumption by calculating the spring constant of a single bone osteon. This can be done by summing the spring constants of all the fibers within an osteon using Equation 1, which is reproduced below.

$$k = \frac{F}{y} = \frac{Gd^4}{8D^3 N_A} \tag{1}$$

The shear modulus from the optimized hierarchy is used. The diameter of the spring will vary based on the lamellar layer. This model will assume a lamellar thickness of 2.5 μm. The number of coils will depend on the fiber orientation and the height of an osteon. We will assume half of the fibers are oriented at 30°, half of the fibers are oriented at 60°, and that an osteon is 5 mm tall. This fiber orientation is similar to that of the preferential fiber model presented for cortical bone. Additionally, the number of fibers contained within each lamella is defined by the circumference of the layer and the diameter of the fiber. We will assume a fiber diameter of 2.10 μm, which was derived from the optimized model. We can then find the spring constant of each lamellar layer by multiplying the individual spring constant of a single fiber by the number of fibers within the layer. The total spring constant of the osteon can be found by summing the spring constants of the lamellar layers. The Young's modulus of the osteon can then be found by applying Equation 2. The resulting longitudinal Young's modulus is found to be approximately 170 KPa.

This model produces very small values for the expected stiffness of cortical bone. The results are more than two orders of magnitude less that what we would expect. For this reason, these early models are discredited.

VI. ADVANCED TOPICS

The models presented in this study analyze the hierarchical relationship of bone. This chapter will serve as an expansion of the models presented earlier. Additionally, this section discusses several topics that are beyond the scope of this study.

A. PRIMARY AND SECONDARY BONE

Primary bone is the initial framework created for the skeletal system. Primary bone is created from the epiphyseal cartilage found near the epiphyseal plate, also known as the growth plate [68]. The mineralization of growing bone occurs rapidly, and less orderly than in secondary bone. This results in very little correlation between collagen structure and mineral deposition [68]. This disordered bone is very similar to woven bone and is generally stronger than secondary bone [116]. Secondary bone is formed when primary bone is resorbed and new bone is deposited. Osteoclasts resorb bone while osteoblasts deposit bone [71]. Deposition of bone is directed by the stresses and loading applied to the bone [116]. This occurs at a cellular level through mechanosensation, which allows the production of new bone to match the local mechanical environment [64]. These processes occur naturally to remove old bone and to repair injuries.

There are two responses to bone injury: repair and regeneration [117]. Initial repair is completed through quickly grown woven bone. This acts as a temporary solution until regeneration occurs. Regeneration serves to replace the injured bone with secondary bone, effectively returning it to its original state. However, there are limits to bone regeneration. Wounds that are too large may never heal [117]. It is in these scenarios when medical solutions can aid in recovery.

B. SYNTHETIC TISSUE GROWTH

The ability to create a lab grown biomimetic bone substitute has profound medical implications. Since bone is a regenerative material, most injuries will heal themselves. However, the healing process is very long and requires setting the bones in the proper positions. Current solutions to broken bones include metal rods, plates and screws that

secure the broken bones in the proper locations. The process can be accelerated through bioresorbable scaffolds [118]. These scaffolds are made of organic and inorganic materials that can be broken down by the body's osteoclasts. Once the scaffolding is resorbed, new bone is laid down.

Research is currently being done into the feasibility of synthetic bone grafts, yet, reproducing the hierarchical structure of bone has proved difficult. The most difficult hierarchy to achieve is intrafibrillar mineralization [68]. The process is directed by proteins within the gap zone that are not present in laboratory conditions. The lack of cell regulated growth has limited laboratory results.

There are several factors influencing synthetic bone composition. Three major goals of scaffold material are biocompatibility, biodegradability and osteoconductivity [119]. Biocompatibility allows the scaffold to interact with the surrounding bone, biodegradability allows it to be broken down by the osteoclasts and osteoconductivity allows bone structure to form properly. These properties are highly depended on the nano-structure of the synthetic bone [119]. In order to mimic natural bone structure and strength, the properties of bone at every level should be understood.

C. AGE AND DISEASE

Both age and disease can affect the structure of bone, the effects of which are often similar. The most common bone disease is osteoporosis. Osteoporosis is a disease that results in reduced bone mass and density. This reduction of bone mass and density has a greater impact on trabecular bone than on cortical bone. The highly porous structure of trabecular bone leads it to be more metabolically active. In bone disorders, this activity leads to greater absorption rate than deposition rate, effectively reducing bone mass. This can result in both trabecular thinning and trabecular loss [120]. Trabecular thinning results in reduced radii of trabeculae while trabecular loss is the complete perforation of trabeculae that results in the loss of a strut. Of these two mechanisms, trabecular loss has a more profound impact on mechanical strength.

Age and disease affect individuals differently and little is known about the cause of age-related bone loss [89]. General trends linked to gender are observed with bone

loss. Bone loss in females is linked to a decrease in estrogen; the decrease of estrogen associated with menopause increases osteoclast activity [89]. This increases absorption in relation to deposition, causing bone loss. In males the onset of bone loss is linked to a decrease of androgen [89]. The onset of bone loss is less rapid in males than in females. In addition to trends with the onset of bone loss, there exist trends with the physical manifestation of bone loss. Females experience greater trabecular loss while males are prone to trabecular thinning [89]. Furthermore, the onset of bone loss begins at different ages for males and females. The process generally starts as a rapid loss in the fifties for women whereas men have gradual onset in their sixties [89].

The model presented in this study analyzed the effects of decreased bone density on the macroscale properties of cancellous bone. A complex FEM could more accurately model the properties of cancellous bone. Not only could the effects of both trabecular thinning and trabecular loss be accounted for, but also the bi-modulus property of trabecular bone.

D. IN VIVO WATER

The presence of water influences the structure and function of living materials, both in their formation and their in vivo state. Mineralization in vivo occurs in an aqueous environment, at atmospheric pressures, and at ambient temperatures [121]. Mineralization occurs after the fibril has formed its structure. The water is tightly packed in a dense liquid phase between molecules and bound within the gap region. BSP is bound within the dense liquid phase near the gap region and nucleates crystal growth. The dense packing of water inhibits final crystal growth but promotes migration of crystal nucleation. This causes the HA crystals to propagate within the gap region and to form small, thin, plates aligned with the fibril [121].

The presence of water affects the properties of biomaterials as well as their formation. Variations in tissue hydration have a profound impact on mechanical properties. This effect is due in part to the structural importance of water. Water helps to bind the TC molecules, providing structural support through hydrogen bonds [122]. The

geometric relationship of TC and HA accounts for the material properties of bone. Abnormalities in geometry can bring about changes in the resulting properties.

Furthermore, the freezing of biomaterials will have an effect on their water phase. This is relevant to posthumous testing of human samples, as almost all samples are frozen for storage. This topic deserves further research.

E. SOFT TISSUES

Biomaterials are not limited to bone, as other soft tissues can be readily identified. Among these, tendons, ligaments, and muscles are the most prevalent.

1. Tendon and Ligaments

Tendons and ligaments are a form of connective tissue. Tendons connect bone to muscle while ligaments connect bone to bone. Tendons and ligaments are responsible for the transmission of tensile loads required for motion in the human body, the restriction of skeletal movement, and the storage of elastic energy [123]. Both tendons and ligaments are hierarchical biomaterials.

The largest structures of ligaments and tendons are fascicles. Fascicles are groups of fibers surrounded by an inter-fascicular matrix [124]. Fibers are themselves a slightly twisting, lattice array of fibrils [123]. Fibrils are an ordered arrangement of collagen molecules. Fibrils exhibit a crimp, which is due to the relaxed state of the collagen molecules. This crimp unfolds when a tensile load is applied to the fibril and reforms when the structure is relaxed [124]. The wavy crimps of the fibrils are aligned, which results in a visible waveform within the fibers [124]. Fibrils are connected through intermolecular cross-linking, as with bone fibrils [125]. This cross-linking produces a periodic banding. The fibrils of tendons are less mineralized than bone, resulting in greater flexibility and reduced rigidity [5]. Collagen molecules of tendons and ligaments are similar to TC molecules present in bone, as collagen I is the predominant form of collagen. However, the collagen molecules of tendons and ligaments also contain small amounts of collagen II and collagen III [124]. The hierarchy of tendons and ligaments can be seen in Figure 21.

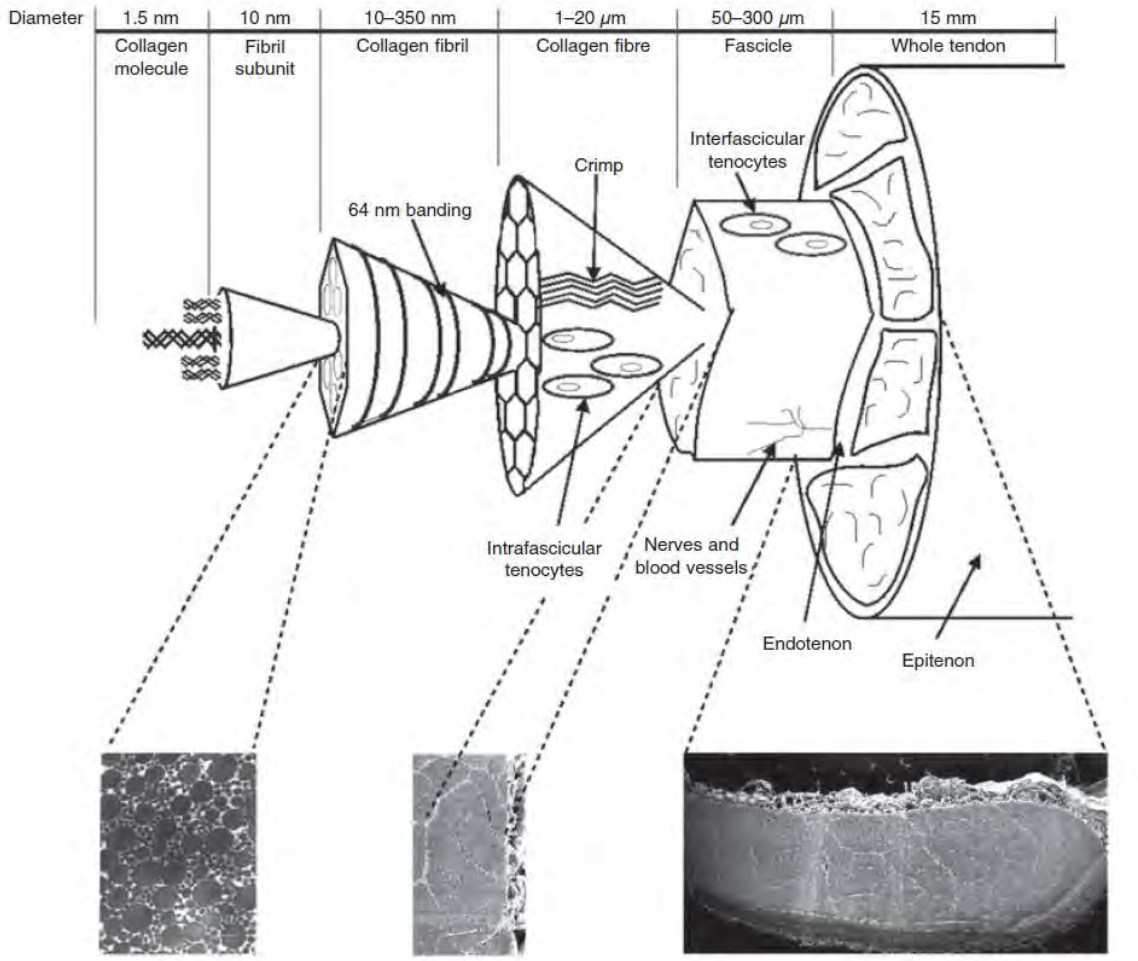

Figure 21. Tendon and ligament hierarchy, from [126]

Tendons and ligaments only transmit tensile loads. Both ligaments and tendons have a high water content, which helps to lubricate individual fibers against longitudinal motion [5]. Additionally, the liquid present in tendons and ligaments has a higher viscosity than the liquid found in bone, allowing for shear forces to be transmitted to proximal fascicles [121]. Furthermore, both ligaments and tendons have limited blood supply and nutritional support, provided through capillary networks. This limited capillary network reduces the void space within tendons and ligaments but also slows healing.

2. Muscle

Muscles are the force producing tissues of the human body. Three types of muscles exist: cardiac muscle, skeletal muscle and smooth muscle [71]. Cardiac muscle exists in the heart and is capable of synchronized contraction. Smooth muscles carry out autonomous motion, such as digestions and organ function. Skeletal muscle is under voluntary control, and is the main motion inducing tissue in the human system. Muscles generate force through contractions [71], and are built upon a hierarchy of structures. The muscle hierarchies can be seen in Figure 22.

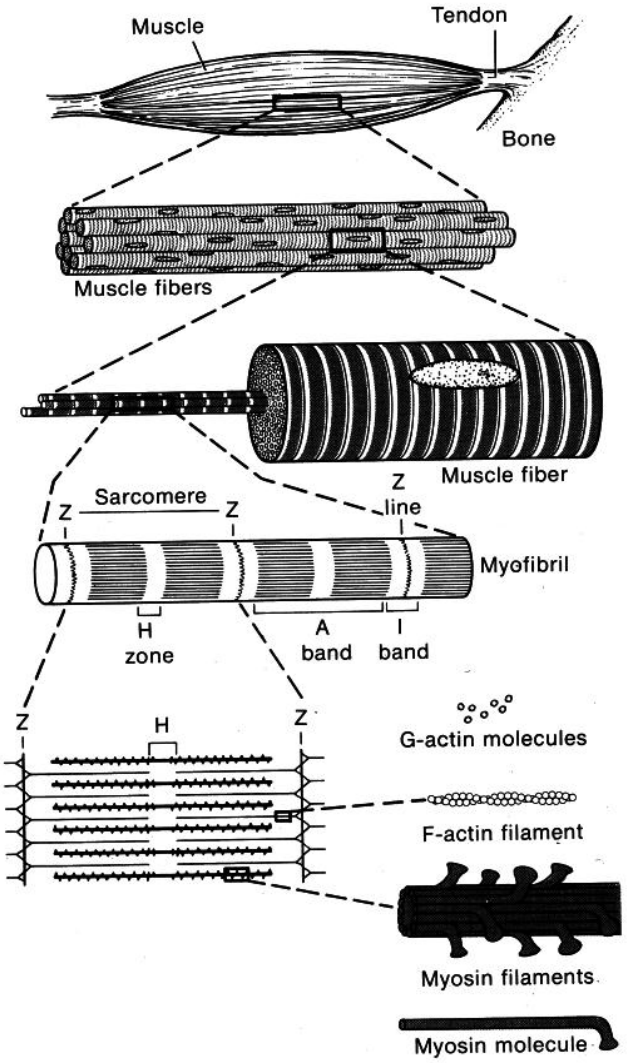

Figure 22. Muscle hierarchy, from [127].

The largest of the structures is a muscle fascicle. Fascicles contain the connective tissue that retains the muscle's shape, houses the blood and nerve supplies, and encircles muscle cells [71]. Muscle cells are the next hierarchy of muscles; they are often called muscle fibers. Muscle fibers are surrounded by a sarcolemma, which contains muscle nuclei and mitochondria. These help support the metabolic functions of muscle. Additionally, the sarcolemma aids in signal transmission of the attached nerves. The smallest unit of muscle is the myofibril, which are contained within the muscle fibers.

Each myofibril is surrounded by a sarcoplasmic reticulum that aids in both containing the myofibril and propagating signals from the nervous system. A myofibril is an orderly arrangement of thick and thin filaments [71]. The filaments of muscle are the structures that induce motion. Thick filaments are a twisted array of myosin molecules. These molecules have an attachment point at their ends that connect to the thin filaments. Thin filaments alternate with thick filaments and are made of actin molecules. The actin molecules have a myosin binding site, which allows the thick filaments to bond to the thin filaments. Each thick and thin filament is oriented parallel to the longitudinal axis of the muscle and are symmetrical across their centers [71].

When a signal from the nervous system initiates motion, the thick filaments bond to the thin filaments and pull them inward. This shortens the myofibril length, inducing a tensile force. This action is repeated for all myofibrils, creating motion.

THIS PAGE INTENTIONALLY LEFT BLANK

VII. CONCLUSIONS

The structures of biomaterials are highly dependent on complex geometries. This study has shown that material properties of hierarchical structures can be found by analyzing each level independently. By linking all hierarchies and adjusting parameters, the influence of each level can then be analyzed. Additionally, changes to the geometry at each level can be completed to test assumptions about the structure of bone.

The nanoscale constituents of bone were described and a spring model was utilized to calculate the longitudinal stiffness of tropocollagen. This simple model produced accurate results. Additionally, a unit-cell based micromechanics model was used to analyze the microscale components of bone. Bone fibrils represent a particle reinforced matrix while bone fibers are a fiber reinforced composite. The fibrillar model produced accurate results as compared to accepted values. The fiber model could not be compared to experimental results, so the eight variations tested were carried over to the next hierarchy.

The first macroscale structures of bone are the lamellar layers. These were modeled as a fiber reinforced composite and compared to accepted values of mineral fraction volume. The results disproved the twisting hydroxyapatite fibrillar model. The linear fibril model was utilized for both cortical and trabecular bone. These macroscale structures utilized a layered composite model to calculate their transverse isotropic material properties. The original hierarchy calculated values below what is expected. Cortical bone had a wider gap between the model results and accepted results than trabecular bone.

A simple finite element model of a tetrakaidecahedron was used to model cancellous bone. Utilizing indices found through experimental testing, the volume fractions of bone and trabecular thicknesses were defined for different anatomical locations. The model was shown to accurately predict the properties of cancellous bone.

This study has revealed that the current anatomical knowledge of bone composition and structure is lacking in detail. The control model analyzed the properties

of bone based on the current understanding of bone structure. But this resulted in a low mineral volume fraction and low stiffnesses. By altering the parameters of each hierarchy an optimized material was found that has material properties close to the accepted values.

The current model contains HA within the gap regions of the collagen framework and on the exterior of fibrils as extrafibrillar matrix. However, this study has shown that more HA is present in the microstructures of bone. Intrafibrillar mineralization may exist between the TC molecules of fibrils. This would stiffen the lowest microscale level, which is then compounded throughout the macroscale hierarchy. Alternatively, the extrafibrillar matrix may take up a larger volume percent than believed. This would increase the mineral volume fraction of bone, as shown through Model 4 of the analysis.

Additionally, it has been assumed that the structure of cortical bone and trabecular bone does not vary at the lower hierarchies [9]. Current beliefs attribute the difference in material properties to the varying orientation of lamellar layers. But, this model has disproved that assumption. The accepted results of cortical bone show an average of 17 GPa and 21 GPa for the longitudinal and transverse stiffness, respectively. The accepted results of trabecular bone exhibit approximately 14 GPa for transverse and longitudinal stiffness. The results of the optimized hierarchy show that the upper limit of cortical bone stiffness is 13 GPa and 15 GPa for the longitudinal and transverse directions, respectively. However, trabecular bone exhibits 17 GPa and 24 GPa for longitudinal and transverse stiffness, respectively. The only difference between trabecular and cortical bone, in this study, is the fiber distribution and the volume fraction assigned to void space. Yet, the values for trabecular bone are much greater than cortical bone. This suggests a structural difference at the lower hierarchies.

This model can be used to validate future discoveries about the structure of bone. As technology advances, imaging capabilities will allow the nanostructures of bone to be explored in detail. The discoveries can be checked against this model to assess their impact on macroscale properties. Additionally, the properties of synthetic bone materials can be checked against the hierarchical structure of bone. This would allow for more anatomically beneficial bone grafts.

APPENDIX. TETRAKAIDECAHEDRON FINITE ELEMENT METHOD STIFFNESS AND TRANSFORMATION MATRICES

A. ELEMENT MATRICES FOR THE THREE DIMENSIONAL GLOBAL MATRIX, FROM [101].

$$\left[K^{e}\right]=\begin{bmatrix} K_{11}^{e} & K_{12}^{e} \\ K_{21}^{e} & K_{22}^{e} \end{bmatrix}$$

$$\left[K_{11}\right]=\begin{bmatrix} a1 & 0 & 0 & 0 & 0 & 0 \\ 0 & b1 & 0 & 0 & 0 & b2 \\ 0 & 0 & c1 & 0 & -c2 & 0 \\ 0 & 0 & 0 & a2 & 0 & 0 \\ 0 & 0 & -c2 & 0 & 2*c3 & 0 \\ 0 & b2 & 0 & 0 & 0 & 2*b3 \end{bmatrix}$$

$$\left[K_{12}\right]=\begin{bmatrix} -a1 & 0 & 0 & 0 & 0 & 0 \\ 0 & -b1 & 0 & 0 & 0 & b2 \\ 0 & 0 & -c1 & 0 & -c2 & 0 \\ 0 & 0 & 0 & -a2 & 0 & 0 \\ 0 & 0 & c2 & 0 & c3 & 0 \\ 0 & -b2 & 0 & 0 & 0 & b3 \end{bmatrix}$$

$$\left[K_{21}\right]=\begin{bmatrix} -a1 & 0 & 0 & 0 & 0 & 0 \\ 0 & -b1 & 0 & 0 & 0 & -b2 \\ 0 & 0 & -c1 & 0 & c2 & 0 \\ 0 & 0 & 0 & -a2 & 0 & 0 \\ 0 & 0 & -c2 & 0 & c3 & 0 \\ 0 & b2 & 0 & 0 & 0 & b3 \end{bmatrix}$$

$$[K_{22}] = \begin{bmatrix} a1 & 0 & 0 & 0 & 0 & 0 \\ 0 & b1 & 0 & 0 & 0 & -b2 \\ 0 & 0 & c1 & 0 & c2 & 0 \\ 0 & 0 & 0 & a2 & 0 & 0 \\ 0 & 0 & c2 & 0 & 2*c3 & 0 \\ 0 & -b2 & 0 & 0 & 0 & 2*b3 \end{bmatrix}$$

The variables used in stiffness matrices are: E which represents Young's modulus along the long axis of the element, G which represents shear modulus of the element, A which represents cross-sectional area of the element, I which represents moment of inertia in the axis noted in subscript, and l which represents element length.

$$a1 = \frac{EA}{l} \qquad a2 = \frac{GJ}{l}$$

$$b1 = \frac{12EI_z}{l^3} \quad b2 = \frac{6EI_z}{l^2} \quad b3 = \frac{2EI_z}{l}$$

$$c1 = \frac{12EI_y}{l^3} \quad c2 = \frac{6EI_y}{l^2} \quad c3 = \frac{2EI_y}{l}$$

B. TRANSFORMATION MATRIX, FROM [101].

$$[T]=\begin{bmatrix}
v_1(1) & v_2(1) & v_3(1) & 0 & 0 & 0 & 0 & 0 & 0 & 0 & 0 & 0 \\
v_1(2) & v_2(2) & v_3(2) & 0 & 0 & 0 & 0 & 0 & 0 & 0 & 0 & 0 \\
v_1(3) & v_2(3) & v_3(3) & 0 & 0 & 0 & 0 & 0 & 0 & 0 & 0 & 0 \\
0 & 0 & 0 & v_1(1) & v_2(1) & v_3(1) & 0 & 0 & 0 & 0 & 0 & 0 \\
0 & 0 & 0 & v_1(2) & v_2(2) & v_3(2) & 0 & 0 & 0 & 0 & 0 & 0 \\
0 & 0 & 0 & v_1(3) & v_2(3) & v_3(3) & 0 & 0 & 0 & 0 & 0 & 0 \\
0 & 0 & 0 & 0 & 0 & 0 & v_1(1) & v_2(1) & v_3(1) & 0 & 0 & 0 \\
0 & 0 & 0 & 0 & 0 & 0 & v_1(2) & v_2(2) & v_3(2) & 0 & 0 & 0 \\
0 & 0 & 0 & 0 & 0 & 0 & v_1(3) & v_2(3) & v_3(3) & 0 & 0 & 0 \\
0 & 0 & 0 & 0 & 0 & 0 & 0 & 0 & 0 & v_1(1) & v_2(1) & v_3(1) \\
0 & 0 & 0 & 0 & 0 & 0 & 0 & 0 & 0 & v_1(2) & v_2(2) & v_3(2) \\
0 & 0 & 0 & 0 & 0 & 0 & 0 & 0 & 0 & v_1(3) & v_2(3) & v_3(3)
\end{bmatrix}$$

The vectors utilized in the transformation matrix are based on the direction cosines of the beam elements. v_1 is directed along the long axis of the element. v_2 is directed perpendicular to the long axis of the element. v_3 is perpendicular to both v_1 and v_2. The three vectors are bound in three dimensional space by a v_0 vector, which points toward the origin of the global axes from the starting point of the v_1 vector. The three direction cosine vectors uphold the following equations:

$$v_2 = v_1 \times v_0$$
$$v_3 = v_1 \times v_2$$

THIS PAGE INTENTIONALLY LEFT BLANK

LIST OF REFERENCES

[1] T. J. Vaughan et al., "A three-scale finite element investigation into the effects of tissue mineralisation and lamellar organisation in human cortical and trabecular bone," *J. of the Mech. Behavior of Biomedical Materials*, vol. 12, pp. 50–62, Aug. 2012.

[2] F.-Z. Cui et al., "Self-assembly of mineralized collagen composites," *Materials Sci. and Eng.*, vol. 57, no. 1-6, pp. 1–27, Aug. 2007.

[3] J.-Y. Rho et al, "Mechanical properties and the hierarchical structure of bone," *Medical Eng. & Physics*, vol. 20, no. 2, pp. 92–102, Mar. 1998.

[4] L. T. Kuhn. (2001). "Bone mineralization," in *Encyclopedia of Materials - Sci. and Technology* [Ebrary version]. [Online]. Available: http://app.knovel.com/hotlink/pdf/id: kt00B79NX5/encyclopedia-materials/bone-mineralization

[5] L. L. Hench and J. R. Jones. (2005). "Clinical needs and concepts of repair," in *Biomaterials*, *Artificial Organs and Tissue Eng* [Ebrary version]. [Online]. Available: http://app.knovel.com/hotlink/toc/id:kpBAOTE001/biomaterials-artificial/biomaterials-artificial

[6] R. L. Drake et al., *Gray's Anatomy for Students*, Philadelphia: Churchill Livingstone Elsevier, 2010.

[7] E. Hamed and I. Jasiuk, "Multiscale damage and strength of lamellar bone modeled by cohesive finite elements," *J. of the Mech. Behavior of Biomedical Materials*, vol. 28, pp. 94–110, Dec. 2013.

[8] D. Taylor. (2003). "Failure processes in hard and soft tissues," in *Comprehensive Structural Integrity* [Ebrary version]. [Online]. Available: http://app.knovel.com/hotlink/toc/id:kpCSIV0002/comprehensive-structural/comprehensive-structural

[9] N. Reznikov et al., "Bone hierarchical structure in three dimensions," *Acta Biomaterialia*, vol. 10, no. 9, pp. 3815–3826, Sep. 2014.

[10] J. Y. Rho. (2001). "Hard Tissues, Mechanical Properties of," in *Encyclopedia of Materials–Sci. and Technology* [Ebrary version]. [Online]. Available: http://app.knovel.com/hotlink/ pdf/id:kt00B79NX5/encyclopedia-materials/bone-mineralization

[11] R. Hambli and A. Barkaoui, "Physically based 3D finite element model of a single mineralized collagen fibril," *J. of Theoretical Biology*, vol. 301, pp. 28–41, May 2012.

[12] N. Reznikov et al., “Three-dimensional structure of human lamellar bone: The presence of two different materials and new insights into the hierarchical organization,” *Bone*, vol. 59, pp. 90–104, Feb. 2014.

[13] S. Weiner and W. Traub, “Bone structure: from Ångstroms to microns,” *Bone Structure*, vol. 6, no. 3, pp. 879–885, Feb. 1992.

[14] N. Sasaki et al., “Atomic force microscopic studies on the structure of bovine femoral cortical bone at the collagen fibril-mineral level,” *J. of Materials Sci.: Materials in Medicine*, vol. 13, no. 3, pp. 333–337, Mar. 2002.

[15] Z.-C. Xing et al., “Immobilization of collagen on hydroxyapatite discs by covalent bonding and physical absorption and their interaction with MC3T3-E1 osteoblasts,” *Tissue Eng. and Regenerative Medicine*, vol. 11, no. 2, pp. 99–105, Apr. 2014.

[16] A. Zamiri and S. De, “Mechanical properties of hydroxyapatite single crystals from nanoindentation data,” *J. of the Mech. Behavior of Biomedical Materials*, vol. 2, no. 4, pp. 146–152, Feb. 2011.

[17] L. J. Katz et al., “On the anisotropic elastic properties of hydroxyapatite,” *J. of Biomechanics*, vol. 4, no. 3, pp. 221–227, May 1971.

[18] C. Rey et al., “Bone mineral: update on chemical composition and structure,” *Osteoporosis Int*., vol. 20, no. 6, pp. 1013–1021, Jun. 2009.

[19] A. K. et al., “Molecular mechanics of mineralized collagen fibrils in bone,” *Nature Commun*., vol. 4, Apr. 2013.

[20] S. Ricard-Blum, “The collagen family,” *Cold Spring Harbor Perspectives in Biology*, vol. 3, no. 1, pp. 1–19, Jan. 2010.

[21] M. Tzaphlidou and P. Berillis, “Collagen fibril diameter in relation to bone site. A quantitative ultrastructural study,” *Micron*, vol. 36, no. 7-8, pp. 703–705, Jan. 2005.

[22] M. J. Buehler and S. Y. Wong, “Entropic elasticity controls nanomechanics of single tropocollagen molecules,” *Biophysical J.*, vol. 93, no. 1, pp. 37–43, Jul. 2007.

[23] M. D. Shoulders and R. T. Raines, “Collagen structure and stability,” *Annu. Review of Biochemistry*, vol. 78, pp. 929–958, Jul. 2009.

[24] B. Brodsky and A. V. Persikov, “Molecular structure of the collagen triple helix,” in *Advances in Protein Chemistry*, vol. 70, pp. 301–339, 2005.

[25] A. Bhattacharjee and M. Bansal, “Collagen structure: the madras triple helix and the current scenario,” *Life*, vol. 57, no. 3, pp. 161–172, Mar. 2005.

[26] K. A. Piez and A. Miller, “The structure of collagen fibrils,” *J. of Supramolecular Structure*, vol. 2, no. 2–4, pp. 121–137, 1974.

[27] T. I. Nikolaeva et al., “Collagen type I fibril packing in vivo and in vitro,” *Biophysics*, vol. 52, no. 5, pp. 489–497, Jan. 2007.

[28] M. J. Stevens and P. J. in’t Veld, “Simulation of the mechanical strength of a single collagen molecule,” *Biophysical J.,* vol. 95, no. 1, pp. 33–39, Jul. 2008.

[29] M. J. Buehler, “Nanomechanics of collagen fibrils under varying cross-link densities: Atomistic and continuum studies,” *J. of the Mech. Behavior of Biomedical Materials*, vol. 1, no. 1, pp. 59–67, Jan. 2008.

[30] N. Sasaki et al., “Elastic properties of collagen in bone determined by measuring the Debye-Waller factor,” *J. of Biomechanics*, vol. 46, no. 16, pp. 2824–2830, Nov. 2013.

[31] S. D. Bolboacă and L. Jäntschi, “Amino acid sequence analysis on collagen,” *Bulletin of University of Agricultural Sciences and Veterinary Medicine-Animal Sciences and Biotechnologies*, vol. 63, pp. 311–316, 2007.

[32] K. E. Kadler et al., “Collagen fibril formation,” *Biochemical J.*, vol. 316, no. 1, pp. 1–11, May 1996.

[33] A. Steplewski et al., “Molecular basis of organization of collagen fibrils,” *J. of Structural Biology*, vol. 157, no. 2, pp. 297–307, Feb. 2007.

[34] J. P. R. O. Orgel et al., “Variation in the helical structure of native collagen,” *PLOS One*, vol. 9, no. 2, Feb. 2014.

[35] J. Bella, “A new method for describing the helical conformation of collagen: dependence of the triple helical twist on amino acid sequence,” *J. of Structural Biology*, vol. 170, no. 2, pp. 377–391, May 2010.

[36] S. Schweizer et al., “Influences on the stability of collagen triple-helix,” *Fluid Phase Equilibria*, vol. 362, pp. 113–117, Jan. 2014.

[37] T. I. Nikolaeva et al., “Collagen fibril formation in vitro at nearly physiological temperatures,” *Biophysics*, vol. 57, no. 6, pp. 757–763, Feb. 2012.

[38] A. Gautieri et al., “Modeling and measuring visco-elastic properties: From collagen molecules to collagen fibrils,” *Int. J. of Non-Linear Mechanics*, vol. 56, pp. 25–33, Nov. 2013.

[39] M. J. Buehler, "Atomistic and continuum modeling of mechanical properties of collagen: Elasticity, fracture, and self-assembly," *J. of Materials Research*, vol. 21, no. 8, pp. 1947–1961, Aug. 2006.

[40] S. Vesentini et al., "Molecular assessment of the elastic properties of collagen-like homotrimer sequence," *Biomechanics and Modeling in Mechanobiology*, vol. 2, no. 4, pp. 224–234, Jun. 2005.

[41] N. Sasaki and S. Odajima, "Stress-strain curve and Young's modulus of a collagen molecule as determined by the X-ray diffraction technique," *J. of Biomechanics*, vol. 29, no. 5, pp. 655–658, May 1996.

[42] R. Harley et al., "Phonons and the elastic moduli of collagen and muscle," *Nature*, vol. 267, pp. 285–287, May 1997.

[43] S. Cusack and A. Miller, "Determination of elastic constants of collagen by Brillouin light scattering," *J. of Molecular Biology*, vol. 135, no. 1, pp. 39–51, Nov. 1979.

[44] H. Hoffman et al., "Localization of flexible sites in thread-like molecules from electron micrographs: Comparison of interstitial, basement membrane and intima collagens," *J. of Molecular Biology*, vol. 172, no. 3, pp. 325–343, Jan. 1984.

[45] Y.-L. Sun et al., "Stretching type II collagen with optical tweezers," *J. of Biomechanics*, vol. 37, no. 11, pp. 1665–1669, Nov. 2004.

[46] A. C. Lorenzo and E. R. Caffarena, "Elastic properties, Young's modulus determination and structural stability of the tropocollagen molecule: a computational study by steered molecular dynamics," *J. of Biomechanics*, vol. 38, no. 7, pp. 1527–1533, Jul. 2005.

[47] D. L. Christiansen et al., "Assembly of type I collagen: fusion of fibril subunits and the influence of fibril diameter on mechanical properties," *Matrix Biology*, vol. 19, no. 5, pp. 409–420, Sep. 2000.

[48] D. K. Dubey and V. Tomar, "Understanding the influence of structural hierarchy and its coupling with chemical environment on the strength of idealized tropocollagen-hydroxyapatite biomaterials," *J. of the Mechanics and Physics of Solids*, vol. 57, no. 10, pp. 1702–1717, Oct. 2009.

[49] D. K. Dubey and V. Tomar, "Role of the nanoscale interfacial arrangement in mechanical strength of tropocollagen-hydroxyapatite-based hard biomaterials," *Acta Biomaterialia*, vol. 5, no. 7, pp. 2704–2716, Sep. 2009.

[50] M. J. Buehler, "Nature designs tough collagen: Explaining the nanostructure of collagen fibrils," *Proc. of the Nat. Academy of Sciences*, vol. 103, no. 33, pp. 12285–12290, Jun. 2006.

[51] C. E. Tye et al., "Identification of the type I collagen-binding domain of bone sialoprotein and characterization of the mechanism of interaction," *The J. of Biological Chemistry*, vol. 280, no. 14, pp. 13487–13492, Apr. 2005.

[52] K. Sato et al., "Crystal orientation of hydroxyapatite induced by ordered carboxyl groups," *J. of Colloid and Interface Sci*., vol. 240, no. 1, pp. 133–138, Aug. 2001.

[53] J. D. Chen et al., "Self-organization of hydroxyapatite nanorods through oriented attachment," *Biomaterials,* vol. 28, no. 14, pp. 2275–2280, May 2007.

[54] S. M. Pradhan et al., "Multiscale model of collagen fibril in bone: Elastic response," *J. of Eng. Mechanics*, vol. 140, no. 3, pp. 454–461, Mar. 2014.

[55] I. Jäger and P. Fratzl, "Mineralized collagen fibrils: A mechanical model with a staggered arrangement of mineral particles," *Biophysical J*., vol. 79, no. 4, pp. 1737–1746, Oct. 2000.

[56] M. P. E. Wenger et al., "Mechanical properties of collagen fibrils," *Biophysical J*., vol. 93, no. 4, pp. 1255–1263, Aug. 2007.

[57] F. Yuan et al., "A new model to simulate the elastic properties of mineralized collagen fibril," *Biomechanics and Modeling in Mechanobiology*, vol. 10, no. 2, pp. 147–160, Apr. 2011.

[58] C. A. Grant et al., "Dynamic mechanical analysis of collagen fibrils at the nanoscale," *J. of the Mech. Behavior of Biomedical Materials*, vol. 5, no. 1, pp. 165–170, Jan. 2012.

[59] Y. W. Kwon and C. Kim, "Micromechanical model for thermal analysis of particulate and fibrous composites," *J. of Thermal Stresses*, vol. 21, no. 1, pp. 21–39, Jan. 1998.

[60] M. S. Park and Y. W. Kwon, "Elastoplastic micromechanics model for multiscale analysis of metal matrix composite structures," *Comput. and Structures*, vol. 123, pp. 28–38, Jul. 2013.

[61] Y. W. Kwon and M. S. Park, "Versatile micromechanics model for multiscale analysis of composite structures," *Appl. Composite Materials*, vol. 20, no. 4, pp. 673–692, Aug. 2013.

[62] E. A. McNally et al., "A model for the ultrastructure of bone based on electron microscopy of ion-milled sections," *PLOS One*, vol. 7, no. 1, Jan, 2012.

[63] X. Su et al., "Organization of apatite crystals in human woven bone," *Bone*, vol. 32, no. 2, pp. 150–162, Feb. 2003.

[64] P. Varga et al., "Investigation of the three-dimensional orientation of mineralized collagen fibrils in human lamellar bone using synchrotron X-ray phase nano-tomography," *Acta Biomaterialia*, vol. 9, no. 9, pp. 8118–8127, Sep. 2013.

[65] E. P. Katz and S.-T. Li, "Structure and function of bone collagen fibrils," *J. of Molecular Biology*, vol. 50, no. 1, pp. 1–15, Oct. 1973.

[66] M. B. Schaffler and D. B. Burr, "Stiffness of compact bone: effects of porosity and density," *J. of Biomechanics*, vol. 21, no. 1, pp. 13–16, Feb. 1988.

[67] S. P. Kotha and N. Guzelsu, "Tensile behavior of cortical bone: dependence of organic matrix material properties on bone mineral content," *J. of Biomechanics*, vol. 40, no. 1, pp. 36–45, Jan. 2007.

[68] M. J. Olszta et al., "Bone structure and formation: A new perspective," *Materials Sci. and Eng. R*, vol. 58, no. 3-5, pp. 77–116, Nov. 2007.

[69] A. Faingold et al., "Osteonal lamellae elementary units: Lamellar microstructure, curvature and mechanical properties," *Acta Biomaterialia*, vol. 9, no. 4, pp. 5956-5962, Apr. 2013.

[70] J. G. Skedros et al., "Cement lines of secondary osteons in human bone are not mineral-deficient: New data in a historical perspective," *The Anatomical Record Part*, vol. 286A, no. 1, pp. 781–803, Sep. 2005.

[71] C. L. Stanfield, *Principles of Human Physiology*, 4th ed., San Francisco, CA: Benjamin Cummings, 2011.

[72] J. M. Whitney, *Structural Analysis of Laminated Anisotropic Plates*, Dayton, OH: Technomic Publishing, 1987.

[73] D. G. Kim et al., "Microstrain fields for cortical bone in uniaxial tension, Optical analysis method," *J. of Eng. in Medicine*, vol. 219, no. H, pp. 119–128, Feb. 2005.

[74] D. R. Carter and W. E. Caler, "Uniaxial fatigue of human cortical bone. The influence of tissue physical characteristics," *J. of Biomechanics*, vol. 14, no. 7, pp. 461–470, Feb. 1981.

[75] H. H. Bayraktar et al., "Comparison of the elastic and yield properties of human femoral trabecular and cortical bone tissue," *J. of Biomechanics*, vol. 37, no. 1, pp. 27–35, Jan. 2004.

[76] P. K. Zysset et al., "Elastic modulus and hardness of cortical and trabecular bone lamellae measured by nanoindentation in the human femur," *J. of Biomechanics*, vol. 32, no. 10, pp. 1005–1012, Oct. 1999.

[77] D. T. Reilly et al., “The elastic modulus for bone,” *J. of Biomechanics*, vol. 7, no. 3, pp. 271–275, May 1974.

[78] D. T. Reilly and A. H. Burstein, “The elastic and ultimate properties of compact bone tissue,” *J. of Biomechanics*, vol. 8, no. 6, pp. 393–405, Feb. 1975.

[79] C. H. Turner et al., “The elastic properties of trabecular and cortical bone tissues are similar: results from two microscopic measurement techniques,” *J. of Biomechanics*, vol. 32, no. 4, pp. 437–441, Apr. 1999.

[80] J. Y. Rho et al., “Elastic properties of human cortical and trabecular lamellar bone measured by nanoindentation,” *Biomaterials*, vol. 18, no. 20, pp. 1325–1330, Oct. 1997.

[81] I. V. Knets, “Mechanics of biological tissues. A review,” *Polymer Mechanics*, vol. 13, no. 3, pp. 434–441, May 1977.

[82] W. C. Van Buskirk and R. B. Ashman, “The elastic moduli of bone,” presented at the Joint ASME-ASCE Applied Mechanics, Fluids Engineering, and Bioengineering Conference, Boulder, Colorado, vol. 36, pp. 131–143, Jun. 1981.

[83] H. S. Yoon and J. L. Katz, “Ultrasonic wave propagation in human cortical bone-II. Measurements of elastic properties and microhardness,” *J. of Biomechanics*, vol. 9, no. 7, pp. 459–464, 1976.

[84] J. L. Katz and A. Meunier, “The elastic anisotropy of bone,” *J. of Biomechanics*, vol. 20, no. 11–12, pp. 1063–1070, 1987.

[85] S. C. Cowin and M. M. Mehrabadi, “Identification of the elastic symmetry of bone and other materials,” *J. of Biomechanics*, vol. 22, no. 6–7, pp. 503–515, Feb. 1989.

[86] H. Gong et al. (2010, July 2). An adaptation model for trabecular bone at different mechanical levels. *BioMedical Eng. OnLine* [Online]. 9(32). Available: http://www.biomedical-engineering-online.com/content/pdf/1475-925X-9-32.pdf

[87] L. J. Gibson, “The mechanical behavior of cancellous bone,” *J. of Biomechanics*, vol. 18, no. 5, pp. 317–328, Feb. 1985.

[88] A. Odgaard, “Three-dimensional methods for quantification of cancellous bone architecture,” *Bone*, vol. 20, no. 4, pp. 315–328, Apr. 1997.

[89] I. H. Parkinson and N. L. Fazzalari, “Characterisation of trabecular bone,” *Stud. in Mechanobiology, Tissue Eng. and Biomaterials*, vol. 5, pp. 31–51, Jan. 2012.

[90] D. P. Fyhrie and M. B. Schaffler, “Failure mechanisms in human vertebral cancellous bone,” *Bone*, vol. 15, no. 1, pp. 105–109, Jan.-Feb. 1994.

[91] M. R. A. Kadir et al., "Finite element analysis of idealised unit cell cancellous structure based on morphological indices of cancellous bone," *Medical and Biological Eng. and Computing*, vol. 48, no. 5, pp. 497–505, May 2010.

[92] X. E. Guo and C. H. Kim, "Mechanical consequence of trabecular bone loss and its treatment: A three-dimensional model simulation," *Bone*, vol. 30, no. 2, pp. 404–411, Feb. 2002.

[93] J. C. Runkle and J. Pugh, "The micro-mechanics of cancellous bone. II. Determination of the elastic modulus of individual trabeculae by a buckling analysis," *Hospital for Joint Diseases*, vol. 36, no. 1, pp. 2–10, Apr. 1975.

[94] P. R. Townsend et al., "Buckling studies of single human trabeculae," *J. of Biomechanics*, vol. 8, no. 3-4, pp. 199–201, Jul. 1975.

[95] R. B. Ashman and J. Y. Rho, "Elastic modulus of trabecular bone material," *J. of Biomechanics*, vol. 21, no. 3, pp. 177–181, 1988.

[96] R. Hodgskinson et al., "Hardness, an indicator of the mechanical competence of cancellous bone," *J. Orthopaedic Research*, vol. 7, no. 5, pp. 754–758, Sep. 1989.

[97] J. L. Kuhn et al., "Comparison of the trabecular and cortical tissue moduli from human iliac crests," *J. Orthopaedic Research*, vol. 7, no 6, pp. 876–884, 1989.

[98] K. Choi et al., "The elastic moduli of human subchondral, trabecular, and cortical bone tissue and the size-dependency of cortical bone modulus," *J. of Biomechanics*, vol. 23, no. 11, pp. 1103–1113, 199.

[99] J. Y. Rho et al., "Young's modulus of trabecular and cortical bone material: ultrasonic and microtensile measurements," *J. of Biomechanics*, vol. 26, no. 2, pp. 111–119, Feb. 1993.

[100] Y. W. Kwon et al., "Representative unit-cell models for open-cell metal foams with or without elastic filler," *Materials Sci. and Eng.*, vol. 343, no. 1–2, pp. 63–70, Feb. 2003.

[101] R. E. Cooke, "Finite element modeling of metal foam structures subject to compressive loading," M.S. thesis, Dept. of Mech. and Aerospace Eng., Naval Postgraduate School, Monterey, CA, 2001.

[102] M. Kasra and M. D. Grynpas, "On shear properties of trabecular bone under torsional loading: Effects of bone marrow and strain rate," *J. of Biomechanics*, vol. 40, no. 13, pp. 2898–2903, Apr. 2007.

[103] E. F. Morgan et al., "Trabecular bone modulus-density relationships depend on anatomical site," *J. of Biomechanics*, vol. 36, no. 7, pp. 897–904, Jul. 2003.

[104] D. Ulrich et al., "The ability of three-dimensional structural indices to reflect mechanical aspects of trabecular bone," *Bone*, vol. 25, no. 1, pp. 55–60, Jul. 1999.

[105] S. Majumdar et al., "High-resolution magnetic resonance imaging: three-dimensional trabecular bone architecture and biomechanical properties," *Bone*, vol. 22, no. 5, pp. 445–454, May 1998.

[106] S. Majumar et al., "Correlation of trabecular bone structure with age, bone mineral density, and osteoporotic status: in vivo studies in the distal radius using high resolution magnetic resonance imaging," *J. of Bone and Mineral Research*, vol. 12, no. 1, pp. 111–118, Jan. 1997.

[107] R. Krug et al., "Assessment of trabecular bone structure comparing magnetic resonance imaging at 3 Tesla with high-resolution peripheral quantitative computed tomography ex vivo and in vivo," *Osteoporosis International*, vol. 19, no. 5, pp. 653–661, May 2008.

[108] M. Ding and I. Hvid, "Quantification of age-related changes in the structure model type and trabecular thickness of human tibial cancellous bone," *Bone*, vol. 26, no. 3, pp. 291–295, Mar. 2000.

[109] A. J. C. Ladd et al., "Finite-element modeling of trabecular bone: A comparison with mechanical testing and determination of tissue modulus," *J. of Orthopaedic Research*, vol. 16, no. 5, pp. 622–628, Sep. 1998.

[110] J. L. Williams and J. L. Lewis, "Properties and an anisotropic model of cancellous bone from the proximal tibial epiphysis," *J. of Biomechanical Eng*., vol. 104, no. 1, pp. 50–56, Feb. 1982.

[111] D. R. Carter and W. C. Hayes, "The compressive behavior of bone as a two-phase porous structure," *J. of Bone and Joint Surgery*, vol. 59, no. 7, pp. 954–962, Oct. 1977.

[112] R. Hodgskinson and J. D. Currey, "Young's modulus, density and material properties in cancellous bone over a large density range," *J. of Materials Sci.: Materials in Medicine*, vol. 3, no. 5, pp. 377–381, Sep. 1992.

[113] R. B. Ashman et al., "Anatomical variation of orthotropic elastic moduli of the proximal human tibia," *J. of Biomechanics*, vol. 22, no. 8-9, pp. 895–900, 1989.

[114] B. Liu et al., "The effective Young's modulus of composites beyond the Voigt estimation due to the Poisson effect," *Composite Sci. and Technology*, vol. 69, no. 13, pp. 2198–2204, Oct. 2009.

[115] M. Hahn et al., "Trabecular bone pattern factor - a new parameter for simple quantification of bone microarchitecture," *Bone*, vol. 13, no. 4, pp. 327–330, 1992.

[116] J. D. Currey, "Mechanical properties of vertebrate hard tissues," *J. of Eng. in Medicine*, vol. 212, no. 6, pp. 399–412, Feb. 1998.

[117] A. R. Shrivats et al., "Bone Regeneration," in *Principles of Tissue Engineering*, 3rd ed. San Diego, CA: Elsevier, 2014, pp. 1201–1221.

[118] S. Yunoki et al., "Effect of collagen fibril formation on bioresporbability of hydroxyapatite/collagen composites," *J. of Materials Sci.: Materials in Medicine*, vol. 18, no. 11, pp. 2179–2183, Nov. 2007.

[119] Y. Liu et al., "Effect of nanostructure of mineralized collagen scaffolds on their physical properties and osteogenic potential," *J. of Biomedical Nanotechnology*, vol. 10, no. 6, pp. 1049–1060, Jun. 2014.

[120] D. Ruffoni and G. H. van Lenthe, "Finite element analysis in bone research: A computational method relating structure to mechanical function," in *Comprehensive Biomaterials*, P. Ducheyne, Ed., Oxford: Elsevier, 2011, pp. 91–111.

[121] J. R. Dorvee and A. Veis, "Water in the formation of biogenic minerals: Peeling away the hydration layers," *J. of Structural Biology*, vol. 183, no. 2, pp. 278–303, Aug. 2013.

[122] A. Gautieri et al., "Hierarchical structure and nanomechanics of collagen microfibrils from the atomistic scale up," *Nano Letters*, vol. 11, no. 2, pp. 757–766, Jan. 2011.

[123] B. K. Connizzo et al., "Structure-function relationships of postnatal tendon development: A parallel to healing," *Matrix Biology*, vol. 32, no. 2, pp. 106–116, Mar. 2013.

[124] H. L. Birch et al., "Specialisation of extracellular matrix for function in tendons and ligaments," *Muscles, Ligaments and Tendons J.*, vol. 3, no. 1, pp. 12–22, May 2013.

[125] R. B. Svensson et al., "Mechanical properties of human patellar tendon at the hierarchical levels of tendon and fibril," *J. Applied Physiology*, vol. 112, no. 3, pp. 419–426, Feb. 2012.

[126] C. T. Thorpe et al., "A review of tendon injury: why is the equine superficial digital flexor tendon most at risk?," *Equine Veterinary J.*, vol. 42, no. 2, pp. 174–180, Mar. 2010.

[127] J. J. Sciote and T. J. Morris, "Skeletal muscle function and fibre types: The relationship between occlusal function and the phenotype of jaw-closing muscles in humans," *J. of Orthodontics*, vol. 27, no. 1, pp. 15–30, Mar. 2000.

INITIAL DISTRIBUTION LIST

1. Defense Technical Information Center
   Ft. Belvoir, Virginia

2. Dudley Knox Library
   Naval Postgraduate School
   Monterey, California